Stabilizing DNA G-quadruplexes by thallium(I) and its application for thallium detection

by

Michael Hoang

A thesis
presented to the University of Waterloo
in fulfillment of the
thesis requirement for the degree of
Master of Science
in
Chemistry

Waterloo, Ontario, Canada, 2015

AUTHOR'S DECLARATION

I hereby declare that I am the sole author of this thesis. This is a true copy of the thesis, including any required final revisions, as accepted by my examiners.

I understand that my thesis may be made electronically available to the public.

Michael Hoang

ABSTRACT

Heavy metals such as thallium are dangerous to living organisms and the environment. They are toxic and harmful. The threat of pollution from these metals is ever growing due to increased mining around the world. Thallium is found between mercury and lead in the periodic table. Thallium is considered more toxic than either of these elements. A reason why thallium is so dangerous is because many biological recognition sites are unable to distinguish it from potassium, a critical metal in biology. Conventional methods to detect thallium ions in the environment have their own disadvantages, including being labour intensive, time consuming, and difficult to perform on site, real time, high frequency monitoring. Therefore, it is highly desirable to have selective biosensors for thallium detection.

DNA aptamers are single-stranded DNA molecules that have the ability to bind towards certain targets with high affinity and selectivity. Some DNA aptamers are able to morph into G-quadruplex structures upon binding with certain metal ions. They are attractive for this project because they tend to bind to K^+ with great affinity, an ion similar to Tl^+. By utilizing this property, we hypothesize that new Tl^+ biosensors could be developed. For this project DNA aptamer biosensor designs relying on the G-quadruplex conformation were developed. These included the Förster resonance energy transfer (FRET) based, and the colorimetric based sensors.

The FRET based sensor utilizes one fluorophore dye on each end of the DNA aptamer. Upon binding to the target in a G-quadruplex conformation, the two ends might approach each other, depending on the DNA sequence. A total of nine fluorescently labelled DNA sequences were screened with the PS2.M DNA found to have the highest sensitivity towards Tl^+. The decreased

distance between the two dyes shifts the dominant wavelength of emission. Using this technique a dynamic range of up to 1 mM Tl^+, a linear range between 0 - 300 µM Tl^+, and a limit of detection (LOD) of 59 µM Tl^+ were determined. The sensor was tested for its Tl^+ sensing ability in the presence of over ten times the amount of alkali ions with little interference effect, demonstrating the higher binding affinity of Tl^+. This sensor was sensitive enough to detect Tl^+ in spiked Lake Ontario water samples.

The FRET based sensors demonstrated the feasibility of using PS2.M for thallium detection. A drawback to this method is the expense involved in labelling the DNA probe, and the need for a fluorometer for detection. For these reasons a colorimetric sensor was designed. The colorimetric sensor design is based on the interactions of gold nanoparticles (Au NPs), and single stranded DNA (ssDNA). In the absence of the Tl^+, the flexible ssDNA adsorbs on the surface of Au NPs. Upon the addition of a highly concentrated salt solution, the Au NPs would be protected from aggregation. In the presence of Tl^+ the DNA is folded, inhibiting adsorption on to the Au NPs. The dynamic range of this system appeared to be 1.3 - 80 µM Tl^+, with a linear range of 1.3 - 20 µM Tl^+, 13.61 units/ mM of Tl^+, and a LOD of 4.56 µM Tl^+. The selectivity of Tl^+ over K^+ was similar to what was found in the FRET based sensor.

After exploring the analytical aspect of this system, the fundamental chemical interactions were also studied. Since the hypothesized mechanism for Tl^+ detection for these sensor designs rely on the G-quadruplex aptamer conformation circular dichroism (CD) is a useful technique. CD uses circularly polarized light to measure the chirality of the aptamer-analyte structure. Using this technique we directly analyzed the structural changes of the aptamers in the presence of Tl^+, and

alkali ions. This analysis revealed characteristic absorbance peaks for antiparallel G-quadruplex structures when in the presence of Tl^+ and K^+ ions.

Isothermal titration calorimetry measures the enthalpy of a reaction. Binding reactions often result in exothermic or endothermic effects. Using this analysis technique, a direct measure of binding is possible. From these experiments, the amount of heat released was small. Despite this it was clear that Tl^+ had the highest enthalpy change, supporting the high selectivity for Tl^+.

In summary, a highly selective probe for Tl^+ was identified in this thesis work. Its application in making biosensors and its fundamental binding interactions with Tl^+ have been studied.

ACKNOWLEDGEMENTS

I would like to thank my supervisor, Dr. Juewen Liu, who throughout these two years has guided me with along with the course of my research work. I have learned much regarding critical thinking, experimental planning, and general research work under his tutelage and for that I shall remain forever grateful. I would also like to thank Dr. Guy Guillemette, who has graciously allowed me the use of his circular dichroism spectrophotometer, which was a great importance for this project.

My time during my master's program would not be the same were it not for my colleagues. Thank you, Feng Wang, Biwu Liu, Kiyoshi Morishita, Jimmy Huang, Zijie Zhang, Ziyi Sun, Howard Tsai, and Runjhun Saran, you have all helped me a great deal with different aspects of my research. Without their help, I would not have been to achieve what I have today.

I would also like to show my gratitude towards my family, who have given me so much support over these years. It was with their encouragement, life lessons, and work ethic that inspired me to pursue the Master's program.

DEDICATION

I would like to dedicate this thesis to my parents, Kiet Hao Hoang, and Li Hong Chan; and my brother Jason Hoang.

Table of Contents

List of Figures

List of Tables

List of Abbreviations

ΔH°: Change in enthalpy

3D: Three Dimensional

6-FAM: 6-carboxyfluorescein

CD: Circular Dichroism

DNA: Deoxyribonucleic acid

FRET: Förster resonance energy transfer

GFAAS: Graphite Furnace Atomic Absorption Spectrophotometry

GI: Gastrointestinal

HEPES: 4-(2-hydroxyethyl)-1-piperazine-ethanesulfonic acid

ICP-MS: Inductively Coupled Plasma Mass Spectroscopy

ITC: Isothermal Titration Calorimetry

K_b: Binding constant:

K_d: Dissociation Constants

LOD: Limit of Detection

NMR: Nuclear magnetic resonance

n: Number of binding sites:

NP: Nanoparticles

SELEX: Systematic Evolution of Ligands by Exponential Enrichment

ssDNA: Single-Stranded DNA

TAMRA: 5-carboxytetramethylrhodamine

UV vis: Ultra Violet Visible

Chapter 1: Introduction

Heavy metals

Heavy metals are often described as high density metals (over 4 g/cm^3), many of which have been shown to have toxic effects on the environment even at low concentrations.[1–3] Examples of toxic heavy metals include lead (Pb), cadmium (Cd), mercury (Hg), arsenic (As), and thallium (Tl). Toxic heavy metals are noted for their detrimental health effects on biological organisms. These effects may include: effecting the growth, development, and survival of an organism.[3] The mechanism in which heavy metals may poison and kill cells is linked to their ability to denature proteins.[1] Despite the well-known dangers of heavy metals, they still present a problem because of how easily they infiltrate into the environment. Mining and its processes are often cited as being responsible for this spread due to the ores they extract and the by-products they produce.[2–6] Natural weathering can leach heavy metals off these by-products and ores into the water cycle. Eventually the heavy metals become deposited into the soil, where it can be bioabsorbed by plants, entering the food cycle.[3,4,6,7] For the purposes of this thesis, the aim is to focus our study on the heavy metal thallium, specifically its ionic form Tl^+.

Thallium

Thallium is considered to be amongst the most toxic of the heavy metals. It is found only in trace amounts in the earth's crust.[8,9] In its pure form, thallium is described as a soft, bluish-white metal, and when bonded with other elements (such as bromine, chlorine, fluorine, and iodine) it is colourless. Since its discovery in 1861, this element was already noted for its highly toxic nature.[8,10–13] The lethality of this substance is so effective that it has even been used for murder.[10,11]

Despite its highly noxious nature it is still used as a rodenticide to this day in where its use still is not banned.[10,12–14] This toxicity comes from its similarity to potassium. Many biological reactions are dependent on potassium, but most biological recognition sites are unable to differentiate it from thallium leading to health damaging effects.[15]

Despite the well-known dangers of thallium, it is often less studied than other heavy metals like lead, cadmium, or mercury.[8,16] The reason for this is because thallium is very difficult to detect using classical analytical techniques which have poor sensitivity to this metal.[8] Recently thallium has been shown to be useful in making super conductive materials. The emerging use of this element has raised concerns that it may become a major pollutant in the environment soon.[8] It is necessary to develop new techniques that will be able to detect thallium at a high specificity and sensitivity to ensure the prevention of and quick response to thallium contamination into the environment.

Thallium: Where does it come from? How does it enter the environment?

Only 15 tons of thallium is produced each year globally and yet, 2000 - 5000 tons is mobilized by industrial processes annually.[14] Thallium has been noted to enter the environment in three ways. The first way is due to the mining industry its by-products.[8,13,14] The second method of entry is through air pollution brought on by coal.[8,14] Lastly, thallium may contaminate the environment from natural sources, even in the absence of human activity.[14,17,18]

Thallium is typically discarded from mining or metal refinement processes due to its low economic importance compared to other metals.[8,14] Coal burning power plants are major sources of

atmospheric thallium pollution, thallium's volatility allows it to travel on fly ash.[8,14] Thallium is commonly present in zinc, copper, lead, sulphide ores, and coal sources.[14] These natural sources may migrate into the food chain even in the absence of human activity.[17] Once thallium leaves from its source of pollution, its enrichment into the surrounding area is made possible due to its readily soluble ionic form (Tl^+).

Once dissolved in water, thallium has the ability to travel deeper into the soil.[9] This is further exacerbated by the fact that thallium is soluble enough to remain toxic.[8,9,13] As described earlier heavy metals can be leached off of their sources by weathering, and enter into the soil through the water cycle. From here, Tl^+ may be bioabsorbed by plants, entering the food chain.[8,17,18] The pollution of thallium into the environment and the food chain is such a concern now that several studies on the uptake of thallium in the local flora and fauna have been performed.[16,19–21]

The chemistry of thallium

Thallium has the atomic number of 81.0, an atomic weight of 204.39, and belongs to group 13 of the periodic table.[22,23] The first three ionization potentials of this element are 589.4, 1971, and 2878 kJ/ mol respectively.[23,24] Thallium is capable of having two stable derivatives (Tl^+ and Tl^{3+}).[22] Stable Tl^{3+} compounds are best found in covalent organothallium compounds.[13,22] Tl^+ is typically more stable than Tl^{3+} in aqueous solution.[24,25] Even though it is soluble enough to be toxic, it is actually only weakly soluble in water. The solubility of Tl^+ is so weak that it is unclear whether Tl^+ actually has a constant hydration number in solution. It has been suggested that the stabilization mechanism for Tl^+ in solution is through macroscopic dialectic hydration.[24] Of the two forms, Tl^+ resembles K^+ and Tl^{3+} is closer to Al^{3+}.[8] Tl^+ will be the species focused on for the rest of this thesis.

Relationship with other alkali metals

As mentioned earlier, Tl^+ has similar properties to alkali ions. Observing Table 1 we see that the ionic radius of Tl^+ is close that of K^+ and Rb^+. Observing the same table we see that Tl^+ distinguishes itself from the other alkali metals by its high polarizability electronegativity and electron affinity.[24] The energy of hydration for Tl is similar to K.

Table 1*: Physical properties of thallium(I) and the alkali metal ions. Reproduced from Ref 24 with permission of Elsevier.*

M	**Ionic radii M^+ (Å)**	**Polarizability M^+ ($Å^3$)**	**Electronegativity M^+ (χ^p)**	**Electron affinity**	**Enthalpy of hydration (kcal mol^{-1})**
Li	0.86	0.03	0.98	0.60	-134
Na	1.12	0.41	0.93	0.35	-107
K	1.44	1.33	0.82	0.30	-87
Rb	1.58	1.98	0.82	0.27	-80
Cs	1.84	3.34	0.79	0.23	-76
Tl	1.54	5.2	1.62	0.32 or 1.21	-92

Similarities and differences to potassium

As mentioned in the previous section, thallium(I) exhibits many similarities to alkali metals. Thallium's similarity to potassium has been taken with great interest, due to the biological effects that thallium may elicit once absorbed into the body.[24] Tl^+ and K^+ share similar ionic radii (Tl^+: 1.54 Å, K^+: 1.44 Å) , share the same ionic charge, and have been known to substitute each other in minerals and biological reactions.[26] One example of such, is how Tl^+ can replace Na^+ and K^+ in the glutamate transporter excitatory amino acid carrier.[27] The potassium-like effects of thallium is a topic of interest for researchers who want to understand if the reason for these similarities come down to the ionic radius alone, or if other atomic properties coming into play as well.[26]

The association constants for thallium(I) halides are significantly higher than alkali halides. A comparison of the thermodynamic data for the association of Tl^+ and K^+ with Cl^- and Br^- is made and given in Table 2.[24] The information uses estimated data for potassium halides. We see from the data that the association reaction for Tl^+ is spontaneous ($\Delta G^0 < 0$), but will only be favourable at lower temperatures. The opposite seems true for K^+ compounds, the association reaction is non-spontaneous ($\Delta G^0 > 0$) and favourable only at higher temperatures, or not at all (KBr).

***Table 2**: Thermodynamic data at 25° C for the association reaction: $M_{aq}^+ + X_{aq}^- \rightarrow MX_{aq}$. Reproduced from Ref 24 with permission of Elsevier.*

MX	ΔG^0 **(kcal/mole)**	ΔH^0 **(kcal/mole)**	ΔS^0 **(cal/K*mole)**
TlCl	-0.93	-1.43	-1.7
TlBr	-1.2	-2.45	-4.2
KCl	+24.0	+24.1	+0.4
KBr	+20.7	+20.0	-2.2

Thallium's biological effects

Tl^+, though similar in size and charge to K^+, is capable of binding to some enzymes with ten times greater affinity than K^+.[15] These qualities make Tl^+ a very dangerous ion, as many biological processes are unable to recognize the differences between the two and separate them accordingly. This results in unwanted side reactions, causing bodily harm.

Thallium can be absorbed through the skin, and mucous membranes, but oral ingestion is the most commonly reported.[15,28] Lethal doses have been estimated to be within the range of 10 - 50 mg of thallium per kg of body weight in humans, with toxic symptoms appearing at 6 mg per kg of body weight.[22] Thallium poisoning may affect the gastrointestinal (GI) tract, the nervous system, the skin, the cardiovascular system, and the kidneys.[22] Citizens living near the Lanmuchang Hg-Tl

deposit have suffered greatly in the form of chronic thallium poisoning. Major symptoms of chronic poisoning include: anorexia, headache, pains in the abdomen upper arms and thighs, or in some causes even the entire body.[8] Aside from these symptoms there is also some limited evidence that the chronic intoxication of thallium may affect one's menstrual cycle, libido, and sperm.[8]

Thallium in biochemistry

Tl^+ has been demonstrated to substitute K^+ as a cofactor in cation activated enzymes such as pyruvate kinase, and sodium-potassium-adenosinetriphosphatase ((Na^+ - K^+) ATPase).[8] The binding of Tl^+ in these cases often result in the inactivation of the enzymes in question.[28] Aside from enzymes, this ion has been shown to interfere with disulphide bonds and ribosomal activities.[22,28,29] One source has even stated that thallium may even affect one's ability to produce enzymes, and reduce mitosis.[8]

Current Thallium detection methods

Thallium may be measured using a variety of techniques including: inductively coupled plasma mass spectroscopy (ICP-MS), differential pulse anodic stripping voltammetry, and graphite furnace atomic absorption spectrophotometry (GFAAS).[13] Thallium is more difficult to detect using classical methods which are often less sensitive to thallium than other elements.[8] Thallium concentrations may be directly measured in one of two ways: ICP-MS or GFAAS.[13]

ICP-MS uses high temperature plasma to convert the sample into ions. The information collected from the plasma directly corresponds with elemental content of the sample.[30,31] ICP-MS has been proven to be a very versatile technique for the detection of thallium. It has frequently been used to

measure thallium levels in water and in soil.[9,32] It has even been reported for its use in measuring biological uptake in organisms.[10,21] ICP-MS has been reported to be very suitable for the detection of thallium.[33,34] Methods to improve this technique to detect Tl^+ in seawater faster have been reported.[35]

GFAAS detects trace elements by atomizing the sample into a flame, having a hollow cathode emitting a spectrum through it, and measuring the absorbance spectrum to detect the elemental content of a sample [36,37]. The detection of thallium may be problematic as the volatility the metal prevents the use of high temperatures for thermal pre-treatment.[13,38] Incomplete elimination of organic and inorganic material may also interfere with readings.[13] In order to deal with the difficulties in measuring thallium, samples are often pre-concentrated prior to measurement.[38] Due to these difficulties, there have been efforts to modify the graphite furnace system to increase the sensitivity of the system towards thallium. These modifications include the addition of pallidum, and dicyclohexano-18-crown-6 to the sample.[38–40]

Aside from these classical methods, several novel methods have also been developed for the detection of thallium in recent years. These novel methods include the use of ionic liquid/graphene electrode sensors, functionalized ZnO nanorods, arsenic sulphide glasses, and micro fabricated bismuth film sensors.[41–44] Table 3 documents the LOD of different methods for detecting thallium from different sources, and sampling media.

***Table 3**: A comparison of different techniques for the detection of thallium both classical and novel.*

Method	**Source**	**Sampling media**	**Limit of Detection**
ICP –MS	Aznalcóllar, Spain	Soils Polluted by Pyrite Tailings	0.001 µg/L [9]
	Hubei, China	Human blood	0.003 ng/mL [10]
	Rio Grande do Sul, Brazil	Rice	0.7 µg/kg [21]
	Lanmuchang mining area, Guizhou Province, China	Rocks/ ore	0.02 mg/kg [17]
		Water	0.005 mg/L [17]
		Soil	0.2 mg/kg [17]
ICP emission spectrometry	Juno Beach, Florida USA	Fish liver	2.5 ppm [45]
GFAAS	Candiota mine in Rio Grande do Sul, Brazil	Coal	0.01 µg/g [39]
GFAAS (Palladium modification)	N/A	Spiked Tl^+ Aqueous solution	0.7 ng/mL [46]
GFAAS (dicyclohexano-18-crown-6 modification)	N/A	Waste water	1 ng/ml [38]
Ionic liquid/graphene modified electrode	Hamedan, Iran	River water & tap water	3.57×10^{-10} mol/L [47]
Ion Sensor Based on Functionalised ZnO Nanorods	N/A	N/A	1×10^{-7} M [44]
Thallium(I)-selective sensors based on arsenic sulfide glasses	N/A	N/A	3×10^{-6} mol/L [43]
Novel Disposable Microfabricated Bismuth-Film Sensors	Canada	Lake water	0.6 µg/L [42]

Deoxyribonucleic acid aptamers

Deoxyribonucleic acid (DNA) aptamers commonly refer to single-stranded nucleic acids with high selectivity and binding affinity towards their target molecules. Naturally occurring DNA is made of only 4 different nucleobases: adenine, guanine, cytosine, and thymine (represented as A, G, C, and T when transcribing an aptamer's sequence, please refer to Figure 1 for illustrations).[48]

These bases are linked to a five-carbon sugar (deoxyribose) to form a nucleoside. These nucleosides are linked to a phosphate group (to form a nucleotide) that help them form a biopolymer.[48] Figure 2 illustrates the structure of DNA. Aptamer strands can form secondary structures such as hairpin loops, bulges, or pseudoknots, higher order structures like G-quadruplexes have also been observed.[49]

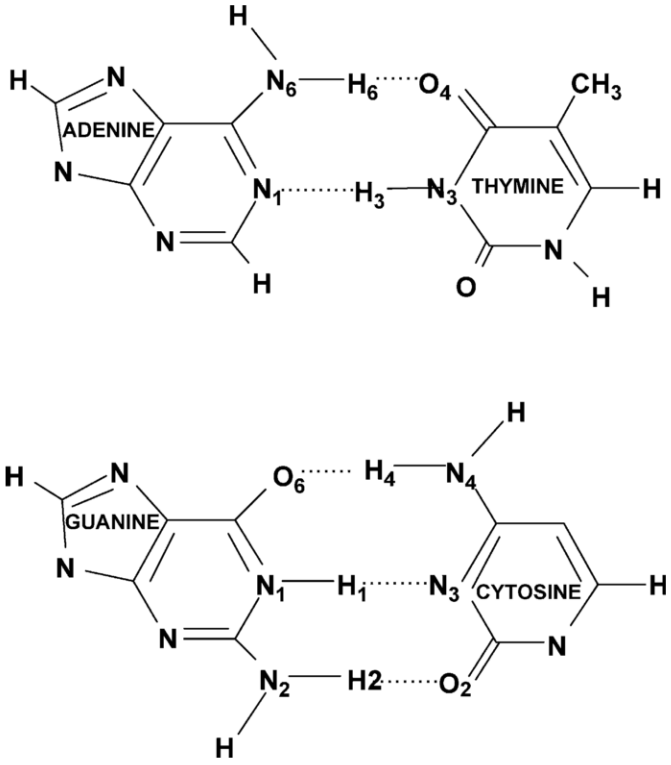

Figure 1*: The chemical structures of the four natural nucleobases (from top left, clockwise), adenine, thymine, cytosine, and guanine, hydrogen bonding with their Watson-Crick pairs. Reproduced from Ref 50 with permission of Elsevier.*

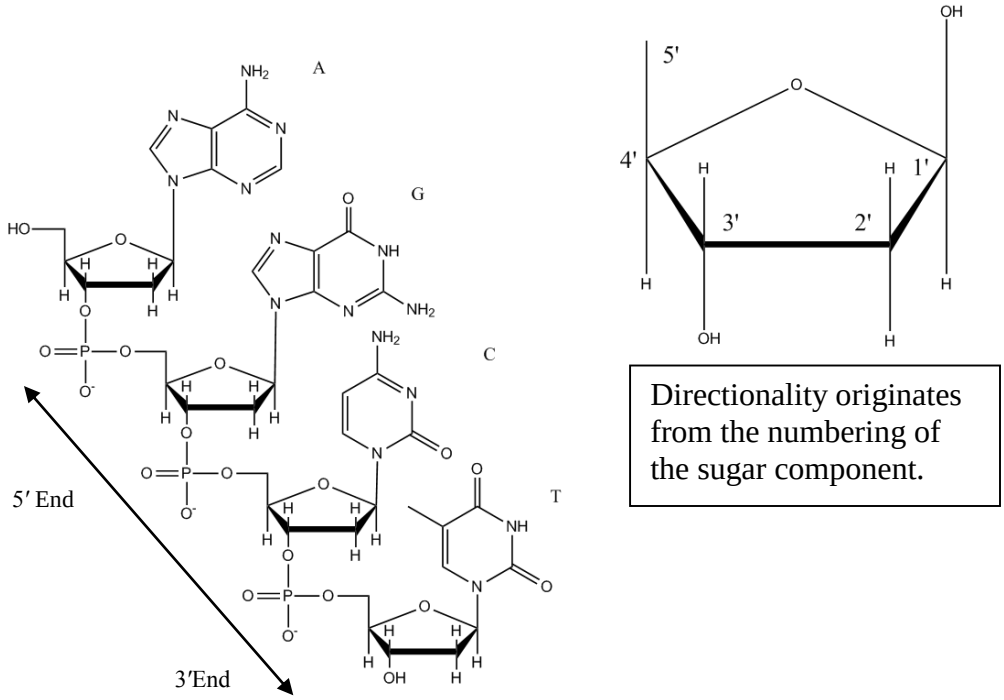

Figure 2*: Nucleotide units connected to form a single strand of DNA.*

DNA aptamers selected for biosensing purposes are most often isolated via systematic evolution of ligands by exponential enrichment (SELEX).[49,51,52] This process makes it possible to isolate a functional strand of DNA that is capable of binding to a single target with high specificity and affinity from a library of approximately 10^{15} sequences.[53] Binding to the target is due to the aptamer's ability to fold into three-dimensional (3D) structures, which allow it to interact with the target using weak forces.[54] The selection process begins with the DNA library incubating with the target of interest during the first step. This is followed by a washing step that removes the unbound aptamers, and then an amplification step that increases the number of successful aptamers. This is repeated several times over (8-15 times) until a DNA sequence with the desired affinity and selectivity is obtained. The separation and isolation of the aptamers are the most vital steps during the selection process.[49,51,52] Figure 3 illustrates the steps involved in SELEX.

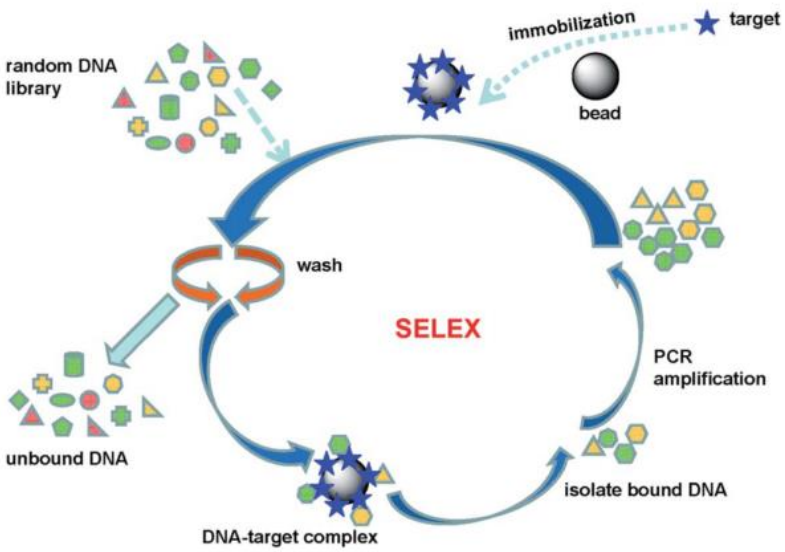

Figure 3*: The steps involved in the SELEX DNA screening process. Reproduced from Ref 55 with permission of The Royal Society of Chemistry.*

DNA binding mechanism

DNA aptamers have a very wide range of binding targets, and when properly selected they may have very high selectivities and affinities towards the target of interest. The selected aptamer typically recognizes and binds to the selected target using a combination of van der Waals forces, electrostatic forces, hydrogen bonding, and base stacking.[49,51,53,54,56] The conformation of the aptamer structure facilitates the interaction of these forces with the target, forming the aptamer-target complex. As the aptamer binds to the target, the aptamer undergoes an induced fit mechanism. Once bound to the target the aptamer adopts a new structure.[53]

The dissociation constants (K_d) for aptamers are typically in the micromolar to picomolar range. These values rival that of antibodies and their interactions with antigens.[53] The high specificity of aptamers makes it possible to discriminate target molecules from their chemically similar derivatives. One report demonstrated an aptamer with 10 000-fold higher binding capacity towards

theophylline over caffeine.[53] The properties of DNA aptamers are thus very attractive in the realm of biosensors and have been used for such purposes.[49]

DNA structures

Free aptamers rarely come unstructured in solution; rather they often adopt a structure based on their sequence and environment. DNA structures are often separated into primary, secondary, tertiary structures, and quaternary structures. Primary structures refer to the DNA sequences themselves.[48,57,58] Secondary structures involve hydrogen bonding, and steric relationships, between bases within the linear structure.[48,58] These relationships may be interstrand, and intrastrand in nature.[58] The tertiary structure is the 3D structure corresponding to these intramolecular forces.[48] Quaternary structures differ from tertiary structures in that they often refer to interactions with other molecules (i.e. other nucleic acids, metabolites, or proteins).[48] These structures are a very important factor in determining the binding affinity towards the target molecule.[59] These structures are determined by the intra and intermolecular forces (hydrogen bonds, hydrophobic effects, and or electrostatic forces).[53]

Typical secondary structures include the stem-loop, the k-turn, and the pseudoknot motifs.[53] K-turn structures have a distinct three-nucleotide bulge, producing a tight kink in helical aptamers. This structure is significant in protein recognition.[53] Loops are commonly seen motifs in aptamer structures. They are often stabilized by mismatch base pairings, and base stacking during target binding.[53] Studies have shown that mismatches may be a significant factor in target recognition, providing possible hydrogen bonds towards the target.[53] Pseudoknots are formed when two stem-loops are nested together.[53] These structures have been found responsible for target binding in some studies.[59]

The G-quadruplex is a tertiary structure formed when a DNA sequence is guanine rich. The mechanism required to produce these structures require four Hoogsteen-paired guanine bases to form a planar guanine tetrad held together via hydrogen bonding.[60] This tetrad stacks upon another tetrad forming the 3D structure known as a G-quadruplex.[53] These structures are often found stabilized by a monovalent or divalent cation in the centre of the quadruplex structure. It has been theorized that this stabilization comes from electrostatic interactions. The effective geometry of a G-quadruplex differs depending on the ion stabilizing it.[53] Figure 4 illustrates the structures described above.

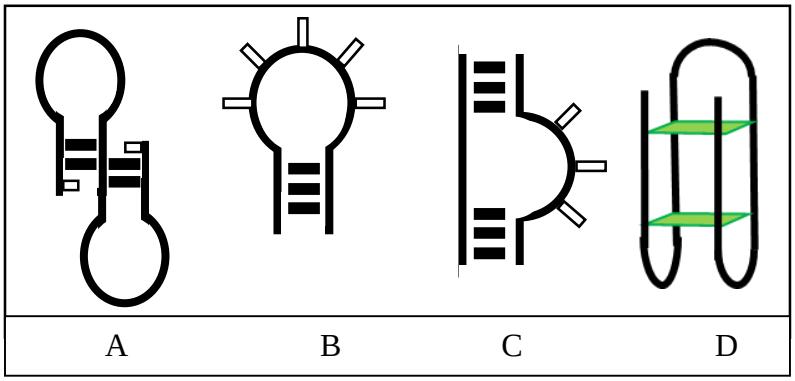

Figure 4*: Possible DNA aptamer structures A) pseudoknot, B) stem-loop, C) k-turn, and D) G-quadruplex. The black bars represent paired bases, while the white bars represented unpaired bases.*

The structure of G-quadruplexes

The structure of guanine makes it capable of forming hydrogen bonds with other molecules of itself, utilizing the N and O within its structure.[61] When four guanines form a tetrad (also known as a G-quartet, see Figure 5), and when at least two or more of these planar tetrads stack (through π-π stacking) upon each other, the resulting structure is the G-quadruplex.[57,60–62] The tetrads are often stabilized by alkali metal ions.[63] These quadruplex structures may be shaped in a variety of ways depending on the number of single-stranded DNA (ssDNA) involved and the folding of each strand. In cases where a single strand of DNA forms the whole G-quadruplex the sequence often

follows that of the following formula: $G_mX_nG_mX_oG_mX_pG_m$, where *m, n, o,* and *p* all represent different integers and X represents any combination of base (G, A, C or T). In this sequence formula we see that the X sequences act as linkers between G-quartets. While the formula implies that the G residues are of equal length this is not always the case, as the linker regions may also contain G residues.[60] G residues in the linker regions may give rise to structures of higher order complexity.[60]

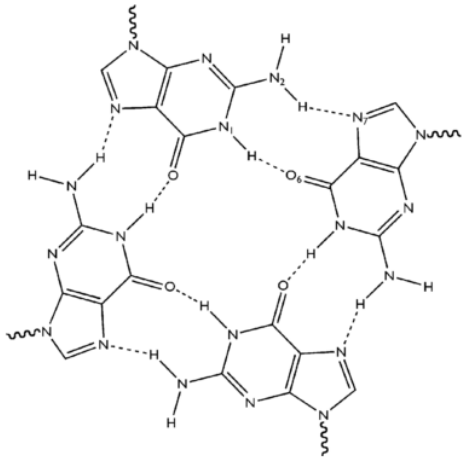

Figure 5*: The structure of the G-quartet, as formed by four guanines. Reproduced from Ref 61 with permission of The Royal Society of Chemistry.*

Each G-quadruplex may be evaluated by the directionality (5′ to 3′) of the strand(s) forming the structure, the conformational state of the glycosidic bond between the guanine and the sugar, and the way the G-quartets are linked together by their linking regions.[61]

G-quadruplexes may be separated into two groups: those with four G-strands running in parallel are called parallel, those with at least one anti-parallel strand are referred to as anti-parallel.[57,61] Different forms of parallel and anti-parallel G-quadruplexes are shown in Figure 6. The structural details used to form the unimolelcular structures will be explained in the next section.

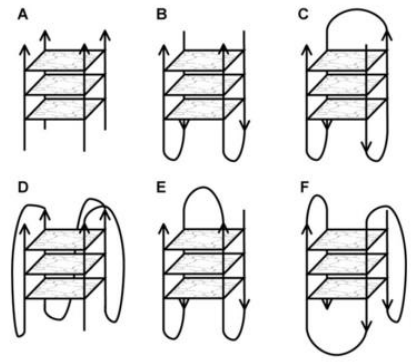

Figure 6*: Possible G-quadruplexes structures. A) parallel tetramolecular structure. B) antiparallel bimolecular structure (with adjacent parallel strands). C) unimolecular antiparallel stand (alternating polarities). D) parallel unimolecular structure with three propeller loops. E) antiparallel unimolecular structure with a diagonal loop. F) antiparallel unimolecular strand with one antiparallel strand. Reproduced from Ref 61 with permission of The Royal Society of Chemistry.*

The glycosidic bond between the guanine base and the sugar may be *syn* or *anti* which is determined by the way the base and sugar rotate in relation to each other (Figure 7).[61] Parallel G-quadurplexes only display *anti* conformations. For anti-parallel G-quaduplexes half of the guanines need to be in the *syn* conformation in order to form the hydrogen bonds necessary. Thus anti-parallel quadruplexes will have *syn* and *anti*-conformations in equal numbers.[60]

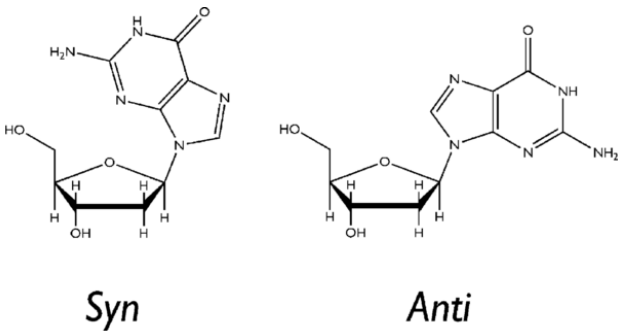

Figure 7*: The two conformations for the sugar-base pair, syn and anti. Reproduced from Ref 61 with permission of The Royal Society of Chemistry.*

The loops formed by the linking regions between G-quartets may be identified as diagonal, lateral, or propeller [60]. Diagonal loops join opposite G-strands.[57,60] Lateral loops join adjacent G-strands.

These two loops connect G-strands in alternating anti-parallel orientations.[57,60] Propeller loops join two parallel stands, connecting in a head-to-head fashion.[57] These loops are dependent on the number of G-quartets, the loop length, the sequence, and sometimes the stabilizing ion(s) used.[60]

Techniques used to analyse the properties of the G-quadruplex include circular dichroism (CD), nuclear magnetic resonance (NMR), and X-ray crystallography. CD spectroscopy could be used to differentiate between parallel and anti-parallel G-quadruplexes. X-ray crystallography and high field NMR spectroscopy may offer more detailed information regarding structure at the atomic level. The last two methods however have limitations regarding the stability of the species being tested.[57]

G-quadruplexes and their interactions with metal ions

The structure of the G-quadruplex is often stabilized by the presence of a metal cation in the centre channel. The mechanism for stabilization has been suggested to be electrostatic in nature, as the cations are positively charged, and the DNA strands are negative.[57,64–66] Specifically the positive charge of the cation counters the negative charge within the cavities in G-quarduplex, thus reducing repulsion.[60,65] The planar G-quartets may be held together by monovalent cations.[61] Ions such as K^+, Na^+, and NH_4^+ interact with the lone pairs on oxygen atoms in the bases surrounding the core.[61,64,67,68] The stability of the structure of depends on the ion(s) used. The stabilizing effect amongst the alkali metals have been ranked in the following manner: $K^+ >> Na^+ > Rb^+ > Cs^+ >> Li^+$.[60,69] Other metals that have been tested include Tl^+, Pb^{2+}, Ca^{2+}, Ba^{2+}, and others, but the results from these studies suggests that they provide less stabilization than K^+.[60] Previous studies

have reported that the exact dimensions and properties of the G-quadruplex structure changes depending on the stabilizing cation.[60]

One study documented the differences in cationic stabilized structures, K^+ favouring parallel structures, while Na^+ tends towards antiparallel G-quadruplexes.[70] The reason for this has been related to their size and how they interact with the structure. The comparatively larger size of K^+ means that it has to be placed in between G-quartets, whereas the Na^+ may locate itself within the centre of the G-quartet.[70]

One study compared how Tl^+ would compare with K^+ in binding with the *Oxytricha nova* aptamer. The effects were tested using NMR. The similarities between the two ions resulted in almost identical quadruplex structures.[57,71] This study also claims that Tl^+ could replace K^+ ions without disturbing the structure greatly.[71]

Another cation of interest is rubidium, whose similarities towards potassium has been noted.[72] Its size is close to that of potassium and thallium, and yet its stabilizing effect is ranked lower than potassium and sodium.[73] The greater size of Rb^+ compared to Na^+ means that when binding to a G-quadruplex it sits between G-quartets just like K^+.[74] The traditional theory for the cation selectivity in G-quadruplex structures was based on the "optimal fit" model. Under this theory K^+ has the optimal size to fit into the space in between G-quartets in a G-quadruplex structure.[66] This would explain why Na^+ has a higher affinity than Rb^+. This theory may be inadequate as calculations performed by other groups have found that the size of K^+ to be larger than the space in between G-tetrads.[66]

Feigon and co-workers have a rationalized that the selective affinity of G-quadruplexes may come down to the free energies of hydration.[66] In order to stabilize the G-quadruplex the and interact with the binding cavity, the ion must be separated from the its surrounding water molecules, effectively dehydrating the ion. A free cation in solution must therefore undergo a dehydration process when stabilizing the G-quadruplex. This theory would explain why G-quadruplexes have lower binding affinities towards Na^+ than K^+, as Na^+ requires more energy to dehydrate than K^+ would.[66] This theory has been tested using different solvents, producing effects that follow the same trends.[66]

Other sources have tried explaining that this selective affinity in G-quadruplexes is a function of both size, and hydration energy.[64,68,75] Larger cations may only fit inside of G-quadruplexes by complexing in between G-quartets (this structure is denoted as G4-M^+-G4). The G4-M^+-G4 structure becomes weaker upon the addition of increasingly larger cations.[68] As the cations become increasingly larger, they become less likely to fit inside the rigid binding cavity inside the G-quadruplex.[76] Despite its larger size, the larger orbital, and electron density of K^+ allow for increased interaction with the tetrads.[68] Thus this theory suggests that smaller alkali metal ions have a high dehydration energy cost that prevents them from binding with the G-quadruplex structure, and that larger ions begin are excluded by steric hindrance.[64,68] After considering hydration effects we see that the stability ranking goes in the reverse.[68]

Examples of heavy metal DNA biosensors

Currently there are many techniques to detect pollutants while maintaining a high level of accuracy, precision, and sensitivity. However many conventional techniques today have the drawback of

being expensive, time consuming, and labour intensive.[56] In order to meet current demands over environmental concern, new techniques are needed in order to provide on-site, real-time, and high frequency monitoring. To do this many researchers have developed sensors that combine biological components, to provide rapid and, accurate sensing.

DNA aptamers are attractive binding molecules because if properly selected they have, high stability, high affinity, high selectivity, ease of modification, and a wide range of targets. For these reasons many researchers have included DNA for many novel biosensor applications.[49,53,56,77]

Metal ion detecting aptamer biosensors have been developed for Mg^{2+}, Na^{+}, Hg^{2+}, K^{+}, Pb^{2+}, Ag^{+} and a few others.[78–83] Metal binding aptamers tend to use three different structures: DNAzymes, DNA mismatches, and G-quadruplexes.[78] DNAzymes are aptamer strands with catalytic properties, using metal ions as cofactors. The reactions they catalyse may act as a signal for ion detection.[78] DNA mismatches have mismatched pairs (like T-T or C-C), that may be stabilized by metals such as Hg^{2+}, or Ag^{+} forming a stable duplex.[78] G-quadruplexes have been elaborated at length earlier in this work. Figure 8 these different aptamer structures.

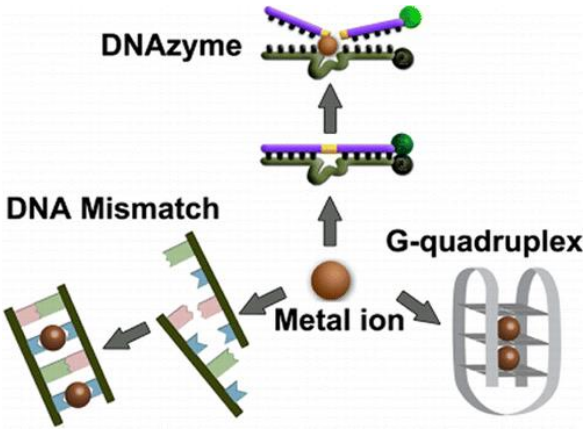

***Figure 8**: A diagram of the various different DNA based metal binding sensor designs. Reprinted with permission from Ref 78. Copyright 2014 American Chemical Society.*

Sensors utilizing G-quadruplexes

As mentioned earlier G-quadruplex structures are stabilized by metal cations. Having already gone over the mechanism in which this structure interacts with the ion, this section will go over the different examples of G-quadruplex metal sensors. Since G-quadruplexes have affinities towards metal ions, they are useful for metal ion detection. Researchers have been able to use G-quadruplexes to detect Hg^{2+}. After binding, K^{+} and hemin are added to solution to create a colorimetric biosensor. Binding to Hg^{2+} prevents the aptamer from binding towards K^{+} and hemin, which would have allowed for a catalytic response leading to a colorimetric signal.[84] Another popular detection method for G-quadruplexes is based on fluorescence signal changes. Some used strands modified with dyes, and some add dyes after binding with the metal cation. In either case a change in fluorescence signal is detected.[85,86]

Research objectives

The objective of this research is to develop new Tl^+ DNA aptamer biosensors. Rationally designing an aptamer sequence for this purpose however, would be difficult. In order to develop a viable sensor, aptamer selection was based off what is known about the K^+ ion. The K^+ ion has the best stabilizing effect for G-quadruplex structures amongst the alkali metals. The stabilizing effects of cations on the G-quadruplex structure has been theorized as electrostatic in nature. Researchers have used this effect to develop K^+ DNA biosensors in the past. One earlier report has documented on how the K^+ and Tl^+ ions induced G-quadruplex structures. As mentioned before Tl^+ has similar properties to K^+, but it tends to have a higher binding affinity towards biological recognition sites. Using these facts, this thesis documents the development of two new Tl^+ DNA aptamer biosensors, utilizing the G-quadruplex structure as the mechanism of detection.

This research aims to develop feasible Tl^+ aptamer sensors. The mechanism of which uses the stabilizing effect of the Tl^+ ion on the G-quadruplex structure. Designs for such sensors include using Förster resonance energy transfer based and gold nanoparticle based colorimetric detection methods. The effectiveness of these designs were verified by experiments that validated each design's sensitivity and selectivity towards the target. Other experiments include circular dichroism, and isothermal calorimetry. The purpose of these tests is to provide a more direct measure of DNA folding, and binding, validating the hypothesized mechanism of the sensor designs.

Thesis outline

This thesis will cover the development of new DNA aptamer based Tl^+ biosensors, their effectiveness, and the tests used to confirm the mechanisms of their detection.

This thesis will be divided into six chapters, the first half of chapter 1 will focus on the dangers, the chemistry and the detection of thallium, the second half will deal with DNA, its properties, its structure, the G-quadruplex structure, and its uses as a sensor. Chapter 2 details the Förster resonance energy transfer-based DNA aptamer sensor design. It is during this chapter that effective Tl^+ binding aptamers were screened. The PS2.M aptamer is the aptamer of main focus for this thesis because of its effectiveness at binding to $Tl^{+.}$ This chapter also covers the tests used to demonstrate the binding affinity, selectivity, and real world sensory applications of the PS2.M DNA aptamer towards Tl^+. Chapter 3 will cover DNA gold nanoparticle based colorimetric detection (using PS2.M), and the tests used to attest the binding affinity and selectivity of this detection system towards Tl^+. Chapter 4 will deal with circular dichroism tests, used to verify the structural changes in DNA aptamers brought about by the addition of cations in to the solution. Chapter 5 details the use of isothermal titration calorimetry to provide a more direct way of measuring binding between the Tl^+ ion and the PS2.M aptamer. Chapter 6 will conclude this thesis with a summery and conclusion of the work done.

Chapter 2: Förster resonance energy transfer-based sensors

Fluorescence is the emission of radiation by a substance that had earlier absorbed a higher energy photon. This effect occurs when an electron absorbs the energy from an incoming high-energy photon, and becomes electronically and vibrationally excited. Some of this energy will be lost as the electron relaxes vibrationally. Afterwards, the electron returns to its original state as it releases a lower energy photon.[87,88]

Förster resonance energy transfer (FRET) denotes a phenomenon whereby the energy of one fluorophore (defined as the "donor") transfers energy to another substance (defined as the "acceptor", or "quencher").[89] The efficiency of this transfer increases the closer they are together .[89–92] This leads to a decrease in the donor's fluorescence, and an increase in the acceptors (if it is also a fluorophore). Figure 9A illustrates an example of this reaction. This reaction may occur if the donor's emission spectrum overlaps with the acceptor's absorbance spectrum, this way the vibrational transitions of the donor will have almost the same energy as the acceptor for the corresponding transitions (Figure 9B).[91]

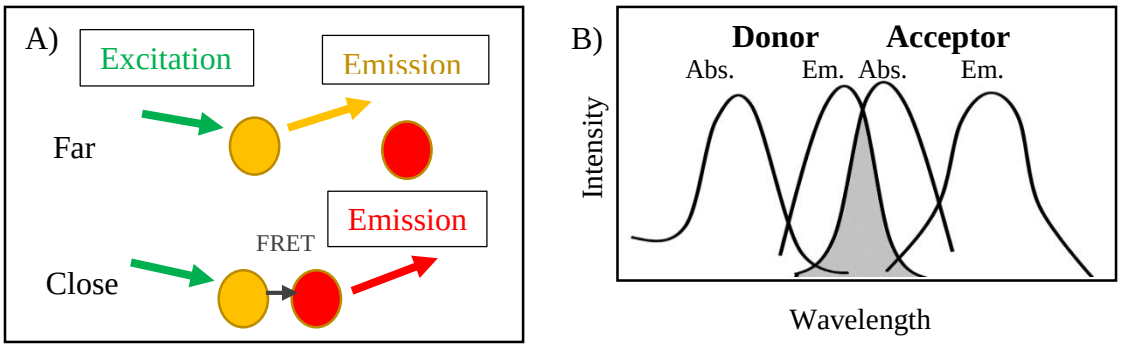

***Figure 9**: A) An illustration of how FRET occurs between the two dyes, at different distances. B) Illustration of the integral overlap needed between the emission spectrum of the donor and the absorption of the acceptor.*

DNA biosensors have exploited this mechanism in the form of molecular beacons. Utilizing FRET, many aptamers have been designed to produce an increase or decrease in fluorescence signal in order to indicate the concentration of an analyte.[93,94] Many of these designs employ a different fluorophore dye on each end. Upon binding to the target, the conformational structure of the aptamer is altered, leading to a change in distance between the dyes, resulting in a signal change .[94] Based on such designs, DNA biosensors for proteins, molecules and ions have been designed.[94] As a result, many different molecular beacons have been developed using a variety of different dyes and aptamer conformations. The intramolecular G-quadruplex structure is of particular interest for this application because once formed, the 5′ and 3′ ends (often labelled with the FRET dyes) are brought into close proximity of each other. This allows for a sensor that can be monitored via FRET signal changes (this mechanism may be viewed in Figure 10).[85] This section will deal with using FRET based G-quadruplex aptamers to detect Tl^+.

Rationale

FRET labelled G-quadruplex forming aptamers are an attractive form of biosensors. Upon their formation the fluorophore and quencher are brought into proximity of each other resulting in a signal change (see Figure 10). In this section Tl^+ is tested against known G-quadruplex forming FRET labelled DNA sequences. As mentioned before Tl^+ is similar to K^+, which has a strong stabilizing effect on G-quadruplex structures. If Tl^+ can do the same thing then aptamer binding can be measured through FRET. Testing for the appearance of G-quadruplex structures using this method have been performed in the past.[61] If a sequence is found to have a high selectivity and affinity towards Tl^+ then this DNA aptamer may have real world applications as a biosensor. This FRET data could be compared to K^+ and the other alkali metals, to act as a control.

Sensor design

In this section, every aptamer used is labelled with a 6-carboxyfluorescein (6-FAM) dye and a 5-carboxytetramethylrhodamine (TAMRA) dye. When the dyes are separated the aptamer emits a 518 nm wavelength (from the 6-FAM) when excited by a 495 nm wavelength. A signal change should occur if binding induces a G-quadruplex structure. When the two dyes come into proximity to each other the emitted wavelength of 518 nm becomes dominated by the 585 nm wavelength (from the TAMRA). Figure 10 illustrates how binding in the presence of Tl^+ may lead to a FRET shift.

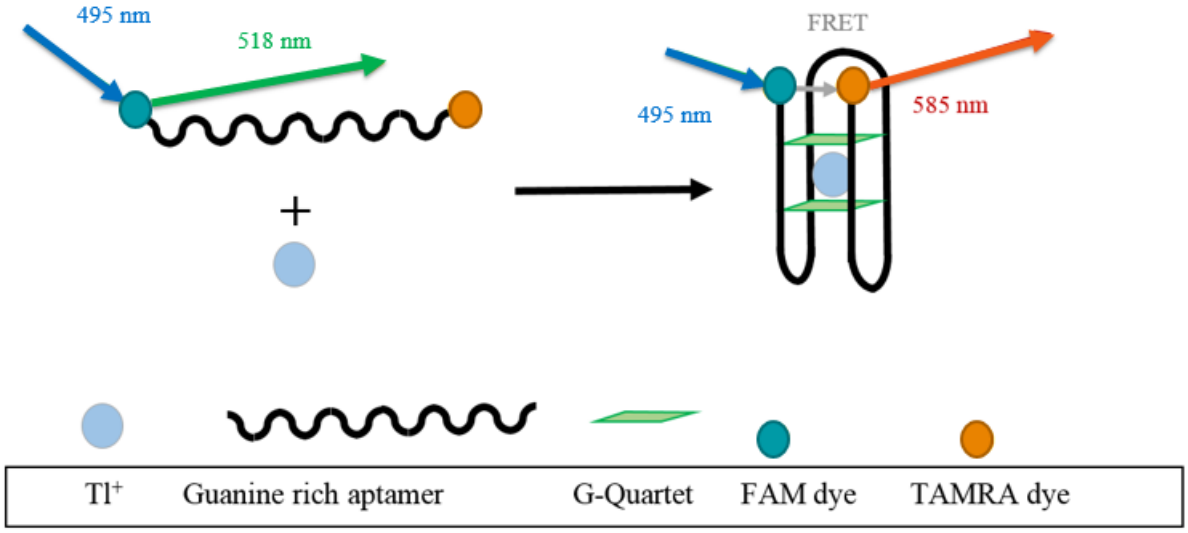

***Figure 10**: An illustration of how a Tl^+ aptamer FRET sensor might work.*

Choice of G-quadruplex forming DNA

Upon starting this project, nine ssDNA sequences were selected and screened for their affinity towards Tl^+. This is done as rationally designing an ssDNA aptamer sequence for this purpose would be difficult. One study has already documented the stabilizing effects of Tl^+ on G-quadruplexes. The selection pool of ssDNA sequences are detailed in Table 4. FT denotes that the

aptamer has a 6-FAM dye and a TAMRA dye at the 5′ and 3′ ends respectively. The first six sequences on the list represent G-rich, quadruplex forming aptamer sequences, the latter 3 were tested to act as a control group. 20 nM of DNA was dissolved in 5 mM 4-(2-hydroxyethyl)-1-piperazine-ethanesulfonic acid (HEPES, pH 7.6) buffer for this experiment. The fluorescence signals were scanned before and after the addition of Tl^+. The response would be calculated as an emission intensity ratio of the at 585 nm signal over the 517 nm one.

***Table 4**: List of ssDNA sequences used for selection.*

Name	**Sequence**
PS2.M-FT	[6-FAM]GTGGGTAGGGCGGGTTGG[TAMRA]
PW17-FT	[6-FAM]GGGTAGGGCGGGTTGGG[TAMRA]
T30695-FT	[6-FAM]GGGTGGGTGGGTGGGT[TAMRA]
K^+-apt-FT	[6FAM]GGGTTAGGGTTAGGGTTAGGG[TAMRA]
AS1411-4-FT	[6-FAM] GGTGGTGGTGGTTGTGGTGGTGGTGG[TAMRA]
AS1411-6-FT	[6-FAM]GGTGGTGGTGGTGGTGGTTGTGGTGGTGGTGGTGGTGG [TAMRA]
Hg-Apt-FT	[6-FAM]TTCTTTCTTCCCCTTGTTTGTT[TAMRA]
Ade-Apt-FT	[6-FAM]ACCTGGGGGAGTATTGCGGAGGAAGGT[TAMRA]
Calib-DNA-FT	[6-FAM]ACGCATCTGTGAAGAGAACCTGGA[TAMRA]

The initial FRET results (no Tl^+) for these nine sequences were quite varied, indicating a wide range of aptamer end-to-end distance distribution. Of the sequences tested, all of them displayed higher FRET efficiency following the addition of Tl^+. The ones with G-rich sequences had more obvious FRET signal changes, than the control sequences. PS2.M-FT had the greatest response, followed by the K^+-apt-FT. The high response to Tl^+ makes these sequences the ideal detection probe candidates. Figure 11 depicts the FRET signal responses of the tested sequences before and after the addition of TlCl. Figure 12 depicts the fluorescence spectrum of PS2.M before and after the addition of TlCl. Figure 13 presents the spectrum results using KCl.

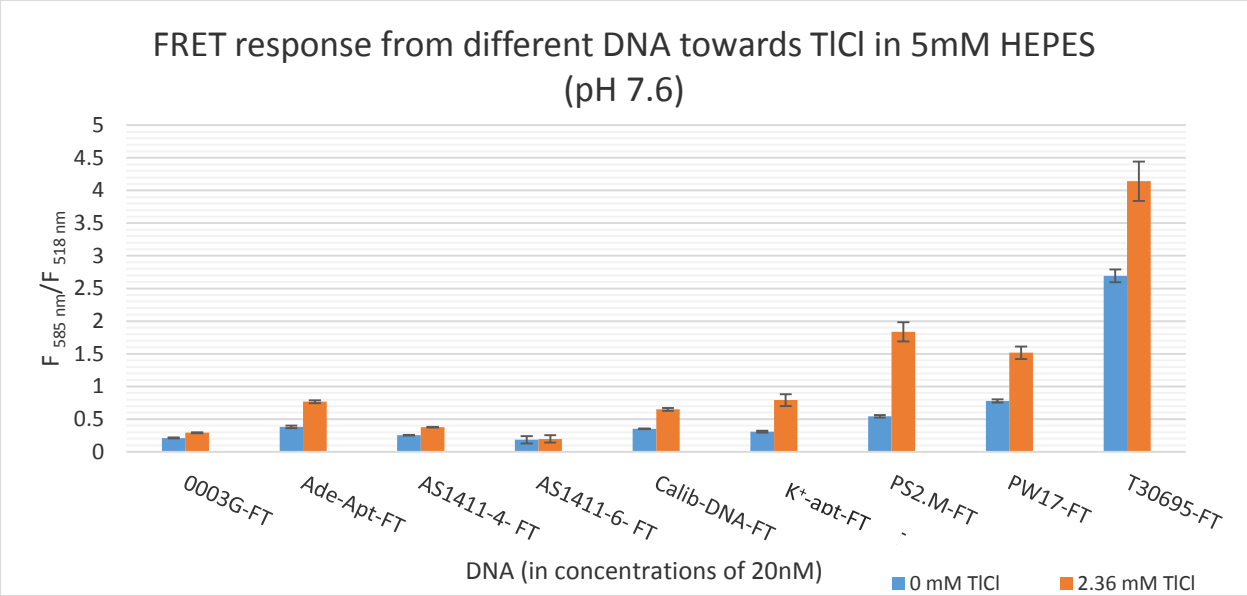

***Figure 11**: A comparison of the signal responses from different FRET labelled aptamers before and after the addition of 2.36 mM TlCl. Buffer conditions: 5 mM HEPES pH 7.6 with 20 nM DNA. Data points were performed in triplicates.*

From the PS2.M spectrum data (Figure 12 and Figure 13) it is clear that TlCl and KCl result in the 518 nm peak being dominated by the 585 nm peak. This indicates that Tl^+, and K^+ are decreasing the distances between the two fluorophore dye ends, most likely due to G-quadruplex formation. The manner that these two ions change the spectrum is different. Tl^+ decreases the 518 nm peak while increasing the 585 nm one. K^+ reduces the 518 nm peak, but does little to the 585 nm peak. The different ways these peaks shift indicate that the binding towards these two ions is different. This difference may be useful for the distinction between these two ions.

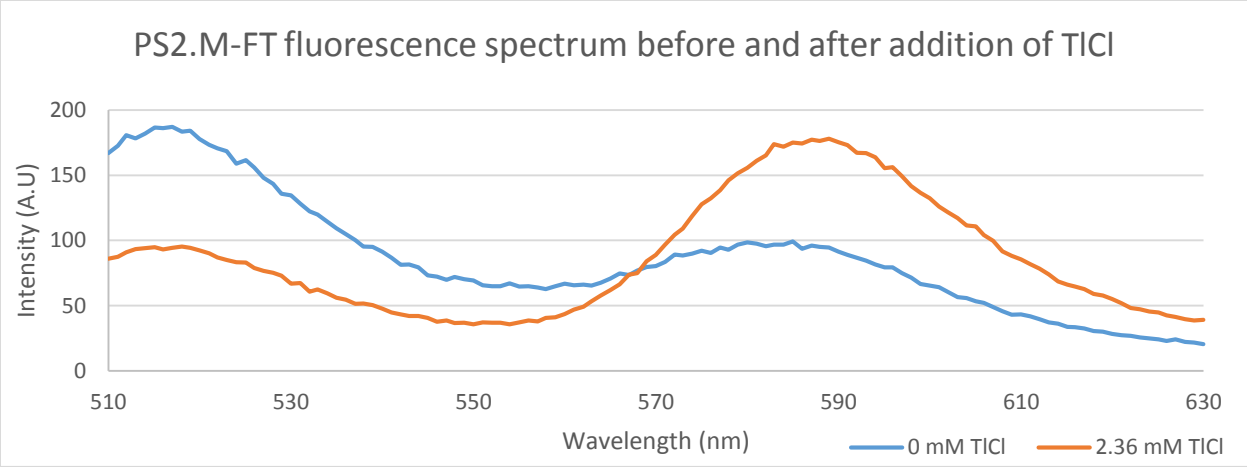

***Figure 12**: The PS2.M-FT fluorescence spectrum before and after the addition of TlCl. Buffer conditions: 5 mM HEPES pH 7.6 with 20 nM DNA (PS2.M-FT).*

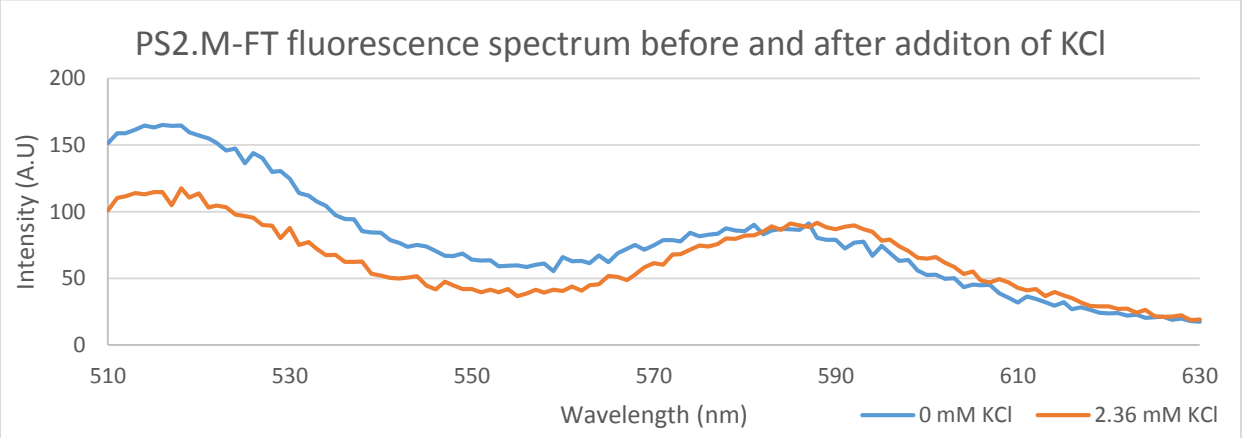

***Figure 13**: The PS2.M-FT fluorescence spectrum before and after the addition of KCl. Buffer conditions: 5 mM HEPES pH 7.6 with 20 nM DNA (PS2.M-FT).*

Optimization of detection conditions

Upon finding suitable DNA aptamers, different buffer conditions and DNA concentrations were tested to identify how they might influence the changes in fluorescence signal. Tested variables included buffer concentrations (Milli-Q water, 5mM HEPES (pH7.6), or 20mM HEPES (pH 7.6)),

and DNA concentrations (ranging from 10 - 50 nM). Aside from these changes, all other steps were consistently carried through similar to earlier.

The results from these tests showed that 5 mM HEPES (pH 7.6) was the best buffer concentration (Figure 14). Minimal effects were observed from different concentrations of FRET DNA (Figure 15). Thus all future tests were performed under the buffer conditions of 5 mM HEPES (pH 7.6) and 20 nM DNA. The results of these tests may be observed.

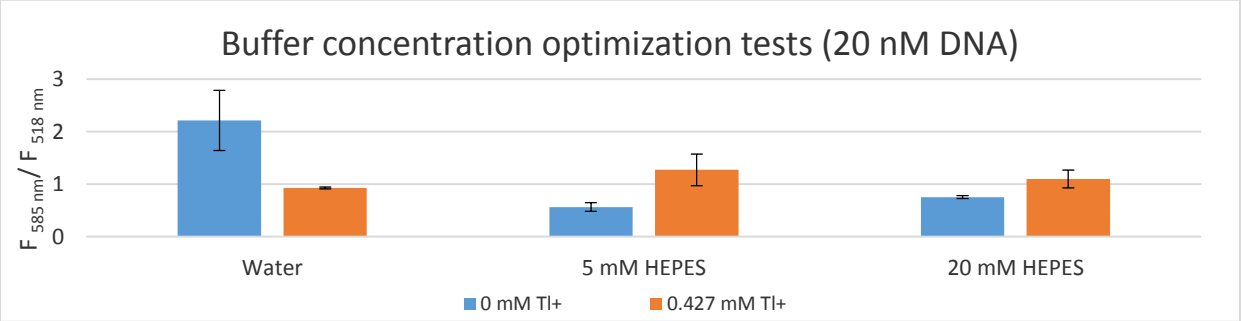

***Figure 14**: Buffer optimization tests. DNA conditions: 20 nM DNA (PS2.M-FT). Data points were performed in triplicates.*

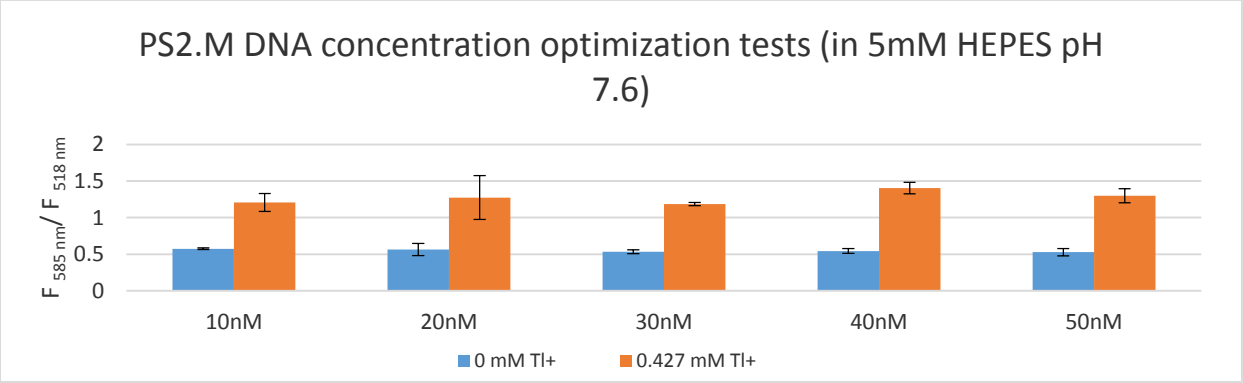

***Figure 15**: DNA concentration optimization tests. Buffer conditions of 5 mM HEPES pH 7.6. Data points were performed in triplicates.*

PS2.M-FT titration

Previous tests have already demonstrated that the PS2.M-FT aptamer has the highest response towards Tl^+; however, this does not deliver any meaningful information on how sensitive or selective it is. To this end, the aptamer was tested against some close analogues to Tl^+. Other metals tested included: Li^+, Na^+, K^+, Rb^+, and Cs^+, for reasons described in page 4. By testing against these different ions, we would be able to demonstrate the selectivity towards Tl^+ against some close analogues.

The titration tests for the PS2.M-FT sensor demonstrated that this sensor had the highest selectivity and sensitivity towards Tl^+ with K^+ coming in second. The response ratios from these two analytes (2.36 mM) were ~1.8, and ~0.9 respectively. The other ions tested showed minimal FRET response (~0.5). Most of the signals indicate a dynamic range of ~1 mM. Our findings are presented in Figure 16. These findings suggest that Tl^+ and K^+ are forming G-quadruplex structures, given their higher stabilizing efficacy. Given the discrimination between the Tl^+ and K^+, this aptamer may still prove to be a useful sensor. Given the high responses from Tl^+ and K^+ the kinetics of these ions binding to the labelled aptamer were studied (Figure 17). Figure 17A details the binding kinetics for PS2.M-FT and Tl^+. Figure 17B details the binding of PS2.M-FT with K^+. In both of these figures, the most characteristic peak shift was studied. In both cases the concentration of the analyte ion was brought up to 2.36 mM after 2 minutes. From the data presented it would seem that Tl^+ binds more slowly to the aptamer than K^+. The time it takes to for the new signal to stabilize was ~1 minute, and ~12 seconds respectively. This might have to do with the higher association constants in thallium halides, than alkali ones.

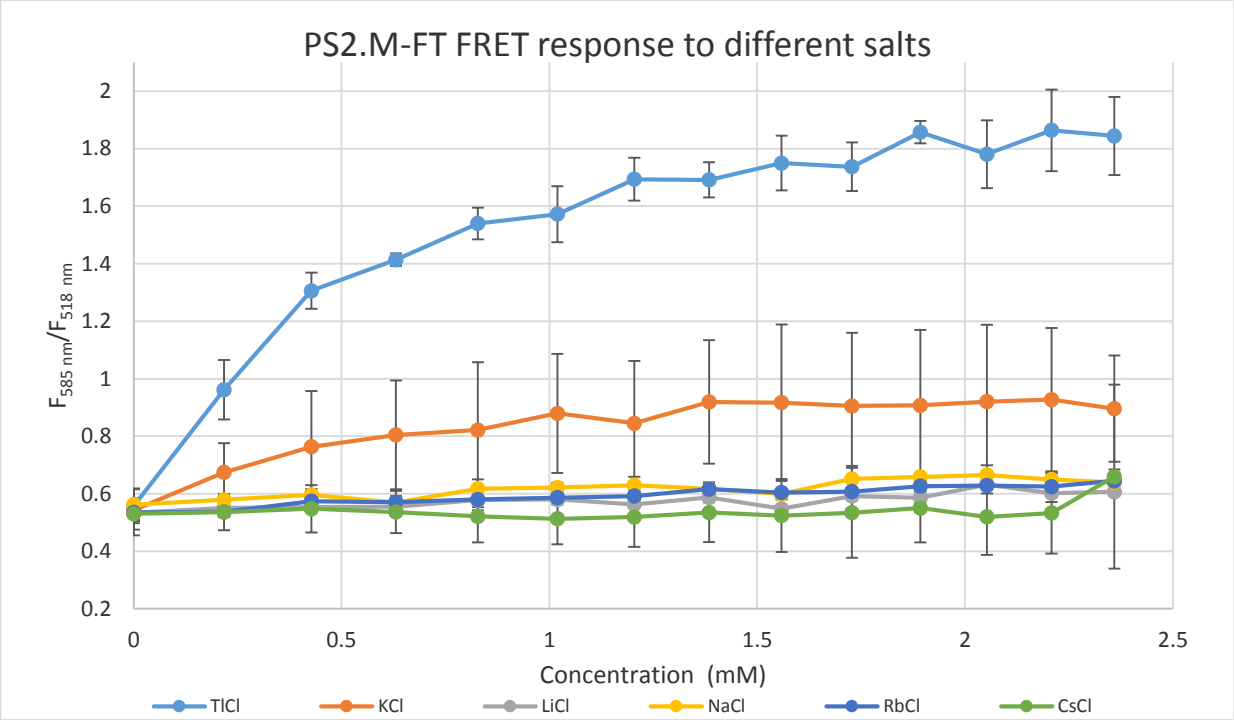

***Figure 16**: PS2.M-FT aptamer response to different ions. Buffer concentration of 5 mM HEPES pH 7.6 with 20 nM DNA. Data points were performed in triplicates.*

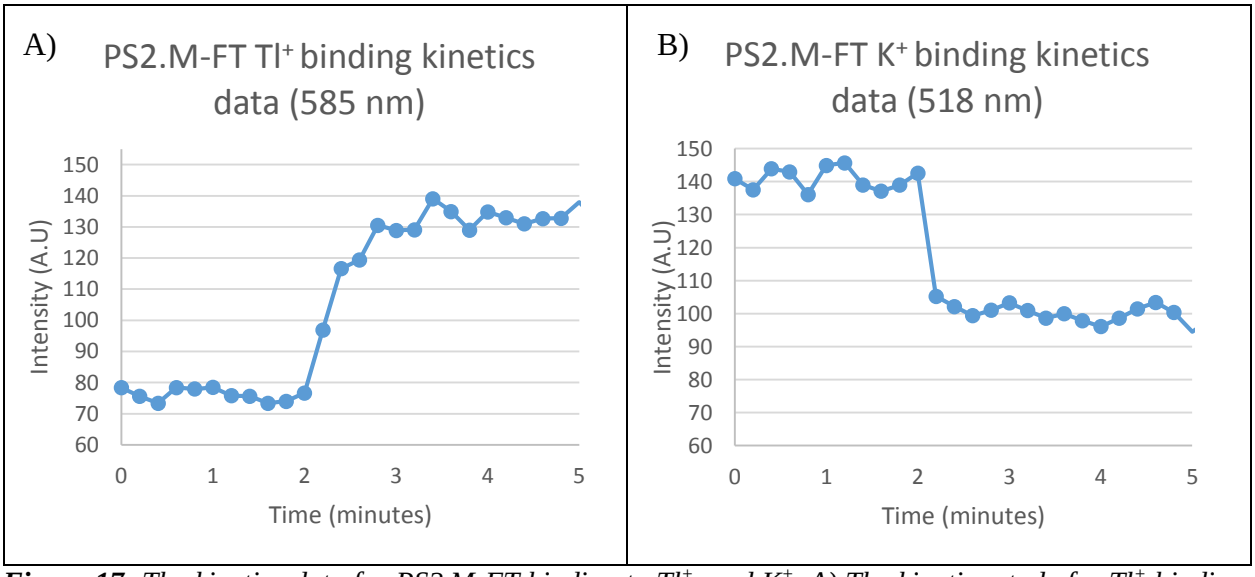

***Figure 17**: The kinetics data for PS2.M-FT binding to Tl^+, and K^+. A) The kinetics study for Tl^+ binding, measuring the 585 nm wavelength. B) The K^+ binding data, using the 518 nm wavelength.*

To demonstrate the discrimination of Tl^{+} over Tl^{3+} a titration test was performed up to 16 µM (owing to insolubility of the Tl^{3+} ion in aqueous solution) these results are presented in Figure 18. This test showed that Tl^{3+} does very little to affect the FRET response of the aptamer.

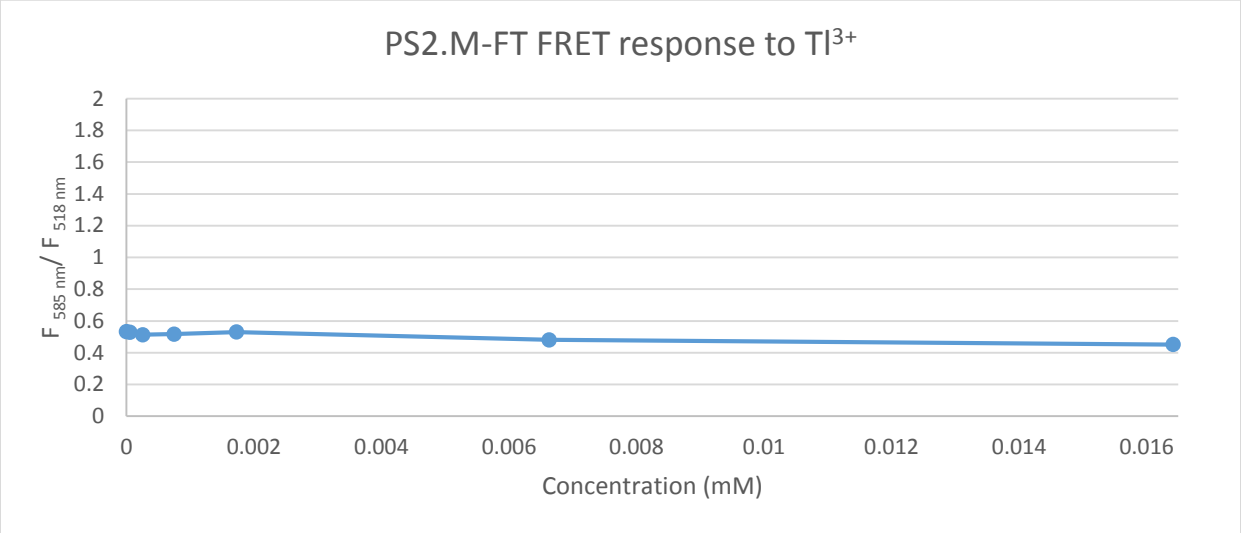

Figure 18: *PS2.M-FT aptamer response to Tl^{3+}. Buffer concentration of 5 mM HEPES pH 7.6 with 20 nM DNA. Data points were performed once.*

PS2.M-FT interference tests

To demonstrate how well this sensor system would be able to handle situations where the Tl^{+} ion would be interacting with other ions, a competitive binding test was performed. Here, the DNA probe would be incubated in a solution of a competing ion (~2.87 mM). One sample containing no competing ion was used as a control. The samples were scanned before and after the addition of 0.217 mM Tl^{+}. These tests showed that Tl^{+} detection unaffected by the presence of other alkali metals. Figure 19 presents these results.

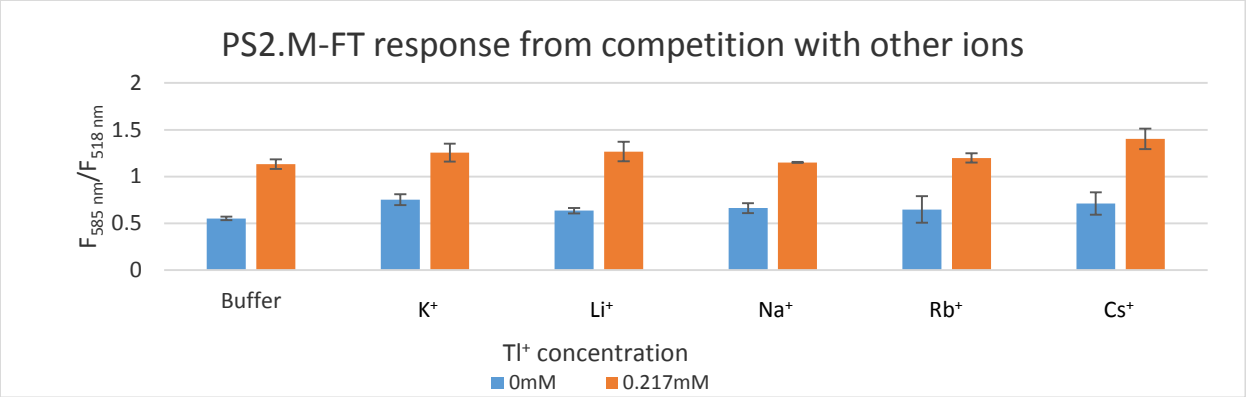

***Figure 19**: Competitive binding tests. Concentration of completive alkali salt in buffer were 2.87 mM. Data points were performed in triplicates.*

PS2.M-FT sensor sensitivity tests

Having better understood the selectivity of this system the PS2.M-FT aptamer was titrated again at lower concentrations, with a greater number of data points. This study found that this FRET based system has a linear range of 0 – 0.3 mM Tl^+, with a sensitivity of 2.48 units/ mM Tl^+, and a limit of detection (LOD) of 0.059 mM Tl^+. Figure 20 document these results.

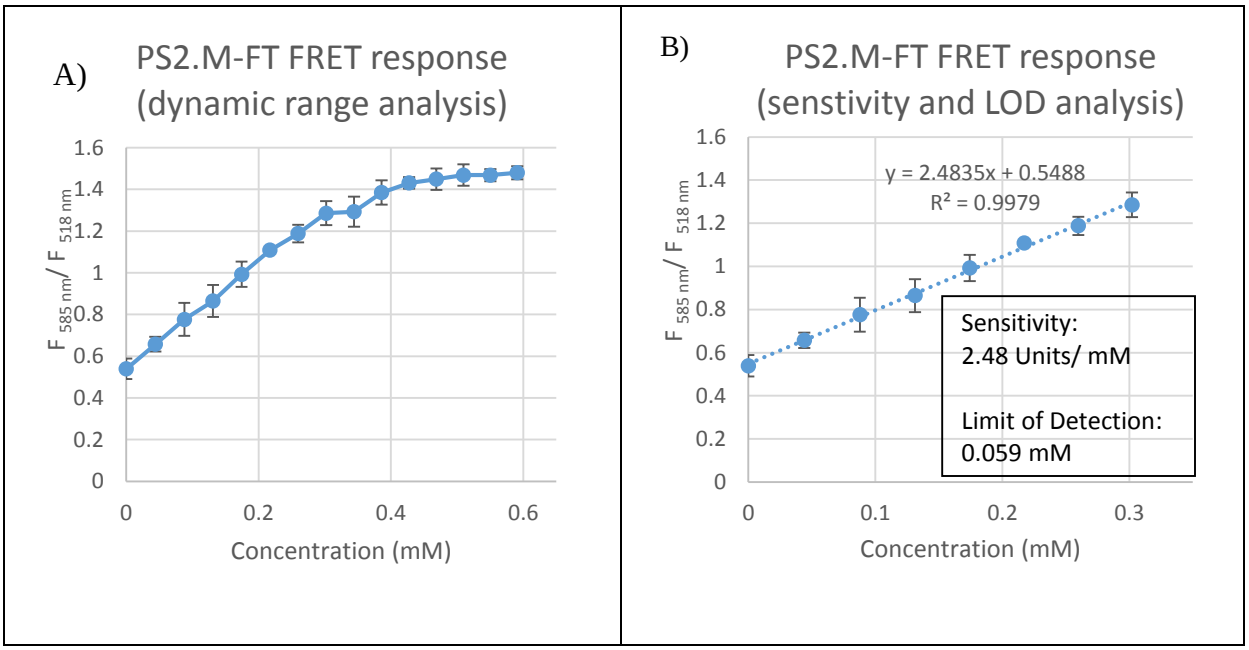

***Figure 20**: FRET response from TlCl titration for PS2.M-FT for A) dynamic range analysis, and B) sensitivity and LOD. Data points were performed in triplicates.*

PS2.M-FT sensor sensitivity tests using Lake Ontario water samples

Given the results for the PS2.M-FT sensor in 5 mM HEPES buffer, a second similar test was performed again using samples of Lake Ontario water. Using the same analysis techniques as earlier we determined that the linear range is approximately 0 – 1.5 mM Tl^+, with a sensitivity of 0.245 units/ mM Tl^+ and a LOD of 0.27 mM Tl^+. From these results, we may infer that the Lake Ontario sample reduced the sensitivity of the aptamer. This could have to do with the components in the components within the water sample interfering with the Tl^+ binding to the aptamer. Figure 21 presents our findings.

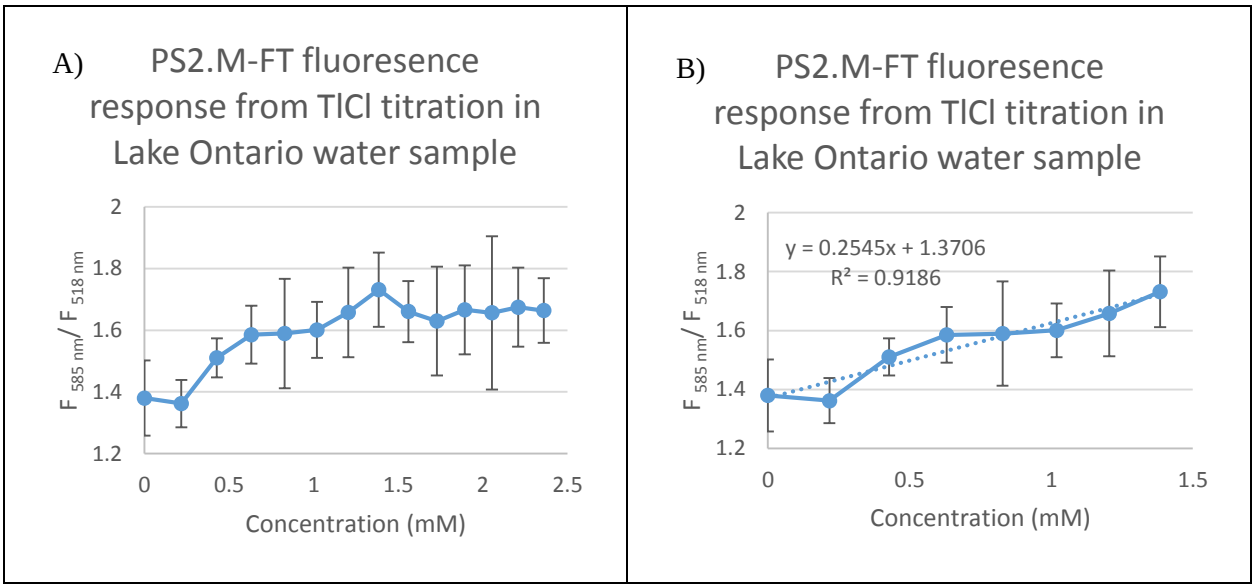

***Figure 21**: FRET response from TlCl titration for PS2.M-FT for A) dynamic range analysis, and B) sensitivity and LOD. Solution conditions 20 nM DNA (PS2.M-FT) in Lake Ontario water. Data points were performed in triplicates.*

K^+-apt-FT sensor titration tests

During the DNA selection tests, it was noted that the K^+-apt-FT aptamer had the second highest response towards Tl^+. Given this, the FRET labelled aptamer was tested under similar conditions to what was mentioned for the PS2.M-FT titration tests. These tests showed that just like the

PS2.M-FT tests, Tl^+ produced the highest FRET response than any of the alkali metals, with K^+ coming in second. It would seem that this aptamer is less selective, given the comparatively high response of K^+. At the highest concentration the selectivity of Tl^+ over K^+ was still less than the PS2.M-FT sensor. Given these results, further tests using this aptamer were not continued. Figure 22 and present the findings from this experiment.

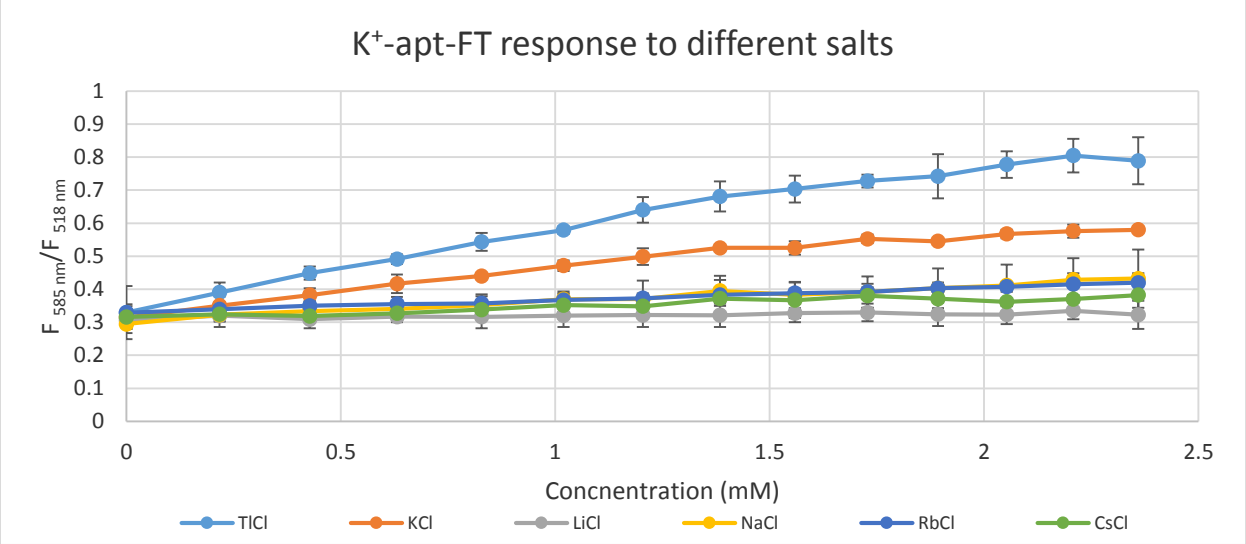

***Figure 22**: K^+-apt-FT aptamer response to different ions. Buffer concentration of 5 mM HEPES pH 7.6 with 20 nM DNA. Data points were performed in triplicates.*

Materials and methods

The materials used for this section were as follows: ssDNA (see Table 4 for details), Milli-Q water, 5 mM HEPES (pH 7.6), thallium chloride, lithium chloride, sodium chloride, potassium chloride, rubidium chloride, and caesium chloride. All experiments were performed at 20^0 C in 5 mM HEPES. All salts were dissolved to a concentration of 13.25 mM in 5 mM HEPES, to act as stock solutions prior to starting the experiment. All measurements were done using the Cary Eclipse Fluorescence Spectrophotometer, using a 1 × 1 cm quartz cuvette. All methods begin with a 3 mL solution of 20 nM DNA in 5 mM HEPES (pH 7.6). The DNA was kept frozen until use.

Selection tests

A 3 mL solution of 20 nM DNA and 5 mM HEPES containing one of the several possible DNA strands would be measured under the fluorometer to act as the baseline. Subsequently 650 µL of 13.25 mM TlCl dissolved in 5 mM HEPES would be added and measured to act as the response signal. All other measurement tests were based off this method.

Optimization of detection tests

The optimization of detection tests was similar to earlier experiments, except the concentrations of DNA, or buffer would be altered accordingly.

Titration tests

The titration tests were similar to the selection tests except the analyte salt solutions would be added 50 µL at a time until a total of 650 µL was added.

Kinetics tests

The kinetics tests were similar to the selection tests except the blank baseline (i.e no analyte) solution was measured for 2 minutes first. Afterwards the analyte sock solution was added to the solution, bringing up the concentration to 2.36 mM. The measurements would continue for another 8 minutes. Measurements were made once every 12 seconds.

Competitive tests

The competitive tests were similar to the selection tests, except the initial solution had ~2.87 mM of analyte solution already. This would be followed by an addition of 50 µL TlCl stock solution.

Conclusions

From the sequences tested for Tl^+ detection it was apparent that the G-rich, quadruplex forming aptamers had an obvious FRET change. Of the G-rich aptamers tested PS2.M-FT and K^+-apt-FT have the highest sensitivity towards Tl^+ with K^+ coming in second. This illustrates the well-known phenomenon of how Tl^+ will bind to the same sites as K^+, but always with a higher affinity. Given how these aptamers are G-rich, how K^+ is noted as having a high G-quadruplex stabilizing ability, and the similarity of Tl^+ to K^+. These high responses are most likely due to G-quadruplex formations.

Of the remaining two, only PS2.M-FT showed a high level of discrimination between Tl^+ and K^+. The sensor demonstrated little response towards other alkali ions, and Tl^{3+}. This aptamer sensor was selective enough to detect Tl^+ in the presence of interfering ions without any significant drops in detection level. The PS2.M-FT kinetics data for Tl^+ and K^+ showed that the signal stabilization was faster for K^+. This might be due to the tighter binding of Tl^+ to halide ions compared to alkali metals. The different fluorescence spectrums of PS2.M-FT before and after the addition of Tl^+ and K^+ possibly indicates different conformation structures depending on the ion.

Sensitivity tests showed that the sensor had a linear range of about 0- 300 µM Tl^+, a LOD of 59 µM Tl^+ and a sensitivity of about 2.48 units/ mM Tl^+ in buffer. This aptamer sensor was even able to demonstrate its sensor properties in real world samples (Lake Ontario water sample) with the dynamic range of approximately 0 – 1.5 mM Tl^+, a sensitivity of 0.245 units/ mM Tl^+ and a LOD of 0.27 mM Tl^+. Given this data, the PS2.M-FT aptamer sensor may have real world Tl^+ sensory applications.

Chapter 3: Colorimetric detection

Previous studies have utilized DNA aptamers, gold nanoparticles (Au NPs, most often 13 nm in size), and highly concentrated NaCl solution to create a label-free colorimetric biosensor.[95–98] The response from this method could be read by the naked eye. The procedure used here was based heavily from the work done in the Rothberg lab.[95] In this section, we hope to demonstrate that the same detection method could be used for Tl^+.

Colorimetric response mechanism

This detection method may be divided into three steps. First, a solution of DNA aptamer and analyte is mixed in buffer. Then a solution of citrate capped Au NPs (13 nm in size, and 13 nM in concentration) is added, which is followed by the addition of highly concentrated NaCl solution.

The reason why this detection method works is because ssDNA aptamers in the absence of their binding target can be quite flexible.[95] Au Np nanoparticles are often made with negative ions adsorbed onto the surface.[95,99] This is to prevent the aggregation of the Au NPs via van der Waals forces. During step two, the flexibility of the unbound aptamers allow them to uncoil and expose their bases, while minimizing the repulsion from their negatively charged phosphate backbones and bind to the surface of the Au NPs. This binding helps further stabilize the Au NPs from aggregating. By adding the salt solution to the mixture, the repulsive charges on the surface of unbound Au NPs are screened, encouraging aggregation amongst the Au NPs. If enough ssDNA strands are bounded to the Au NPs, the solution remains red (Figure 23).

The presence of the target results in a colour change. If enough aptamer-analyte complexes form prior to the addition of the Au NPs, the DNA would not be able to adsorb on the An NPs. This leaves the Au NPs unprotected from aggregating in the presence of high salt concentrations. The structure of the DNA aptamer-analyte complex is too rigid to minimize the repulsive forces from the negatively charged phosphate backbone from the negatively charged surface of the Au NPs.[95,97,98] This relationship between stable structures in DNA and gold adsorption has been documented in the past.[100–102] This results in the Au NPs aggregating, and the resulting solution becomes blue/purple, due to size related surface plasmon resonance effects (Figure 23).[97] This method is advantageous in that it does not require the chemical modification of the DNA aptamers, or instrumentation for analysis, both of which could be expensive.[83,98]

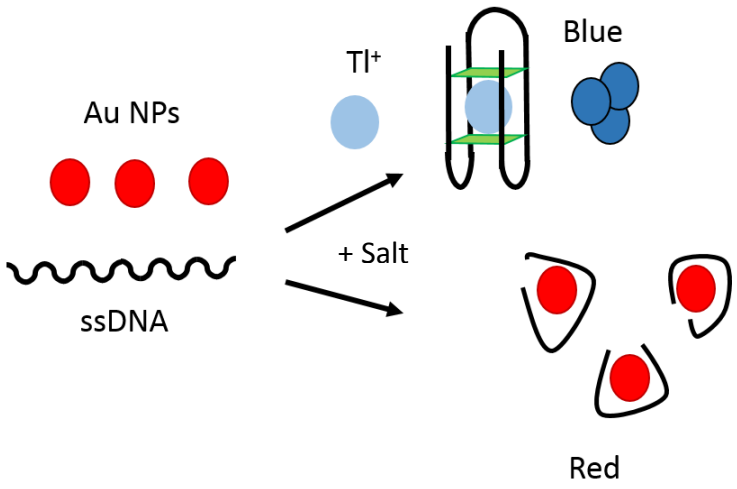

***Figure 23**: Scheme of the colorimetric detection of Tl^+ using the aptamer Au NP detection method.*

Rationale

Similar to the FRET based sensor, the colorimetric detection method provides another way that the PS2.M aptamer may be utilized for Tl^+ detection. The colour changes from this method are due to the aptamers binding to their target sequence, and forming stable structures. By successfully

utilizing the colorimetric method to detect Tl^+, we could demonstrate another possible detection method for the PS2.M aptamer.

This method of detection is advantageous, FRET labelled aptamers are often costly, and require instrumental analysis.[95] For this purpose Au NPs are often employed for this process because of their high extinction coefficient, and aggregation-induced colour changes.[103–105] If the Tl^+ ion is capable of inducing a G-quadruplex structure in the PS2.M aptamer, then the sensor should present this as a colour change from red to blue (the reason for this is detailed below). If the selectivity and sensitivity of this system is found to be high enough, this detection method would be a feasible detection method.

Selectivity tests

The first experiment performed on this system examined the selectivity. The DNA-analyte solution was mixed in a 5 mM HEPES (pH 7.6) buffer. The DNA (PS2.M) concentration prior to the addition of the Au NPs was 20 µM. The analytes used were TlCl, KCl, LiCl, NaCl, RbCl, and CsCl. The analyte concentrations used were 2.65 mM (before the addition of Au NPs), similar to the maximum concentrations used in the FRET experiments. 200 µL of 13 nM 13 nm Au NP solution was added thereafter, followed by 100 µL of 200 mM NaCl (in 5 mM HEPES). Figure 24 is a photograph of the different solutions after the addition of the 200 mM NaCl solution. The first two vials from the left in the photograph are the positive (no DNA) and negative controls (no analyte). Following these tests it was immediately observable that TlCl had the most noticeable colour response out of all the analytes used. While Tl^+ resulted in a purple colour change, the other analytes remained red, just like the negative control. The differences between Tl^+ and the other

alkali ions were visible to the naked eye, suggesting that the other alkali metals produced an insignificant response.

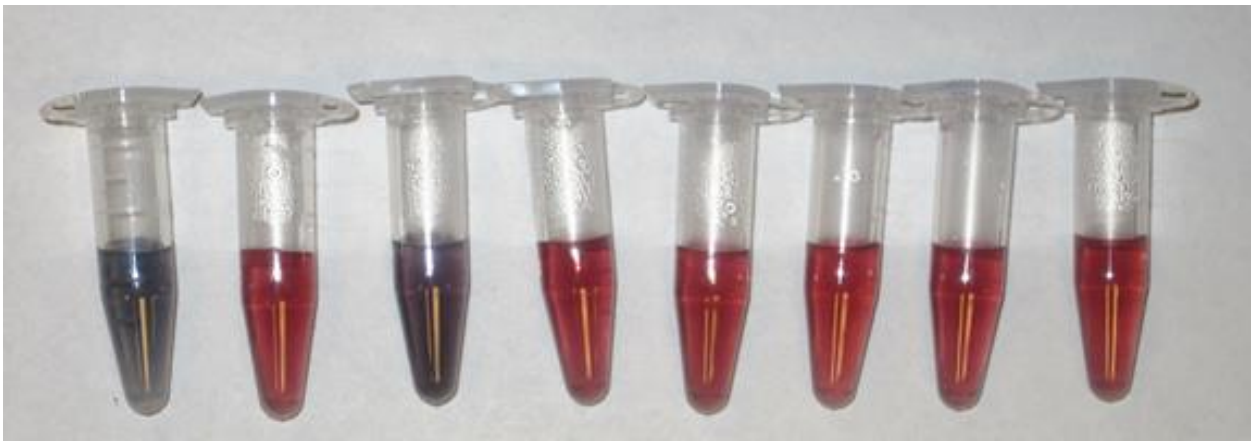

***Figure 24**: Colorimetric tests using Au NPs. From left to right: positive control, negative control, Tl^+, K^+, Li^+, Na^+, Rb^+, and Cs^+.*

Figure 25 displays the ultraviolet-visible spectroscopy (UV-vis) spectrum readings for the sensor, one in the presence of Tl^+ and the other represents the negative control. With the addition of Tl^+, we see a decrease in the 520 nm peak, and an increase in the 650 nm region. These Tl^+ induced shifts allow for ratiometric measurements. The other solutions were also analysed under UV-vis in order to measure the results in a quantitative manner (Figure 26). The response signal was calculated as a ratio of the absorbance values at two wavelengths (650 nm over 520 nm). The results of this method demonstrated that the selectivity over K^+ for this system is similar to the FRET system. Moreover, all of the alkali analytes had absorbance values similar to that of the negative control, suggesting that they produced a negligible response. The positive control tended aggregate very quickly after the addition of salt, and could not be analysed with the rest. Given the level of discrimination this system offers, it may be a viable biosensor. The results seem to indicate that the PS2.M aptamer can only adsorb on to the surface of the Au NPs in the absence of Tl^+, this

is consistent with the mechanism presented in Figure 23, suggesting that Tl^+ binds to the PS2.M aptamer and forms a higher order structure.

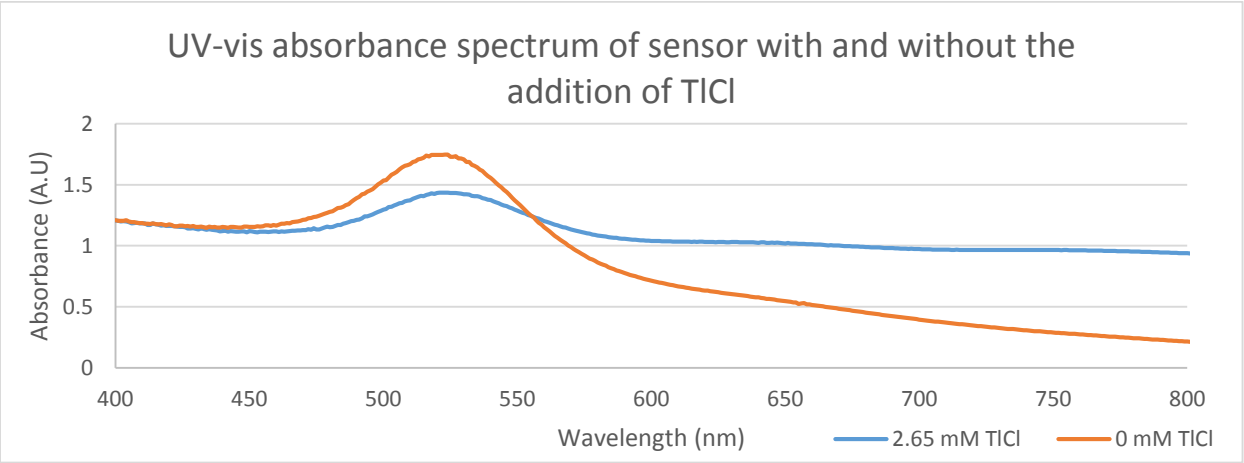

***Figure 25**: UV-vis absorbance spectra for the Au NP colorimetric sensor system. Of the spectra displayed, the blue line represents the spectrum for the sensor exposed to Tl^+ and the orange one displays the negative control.*

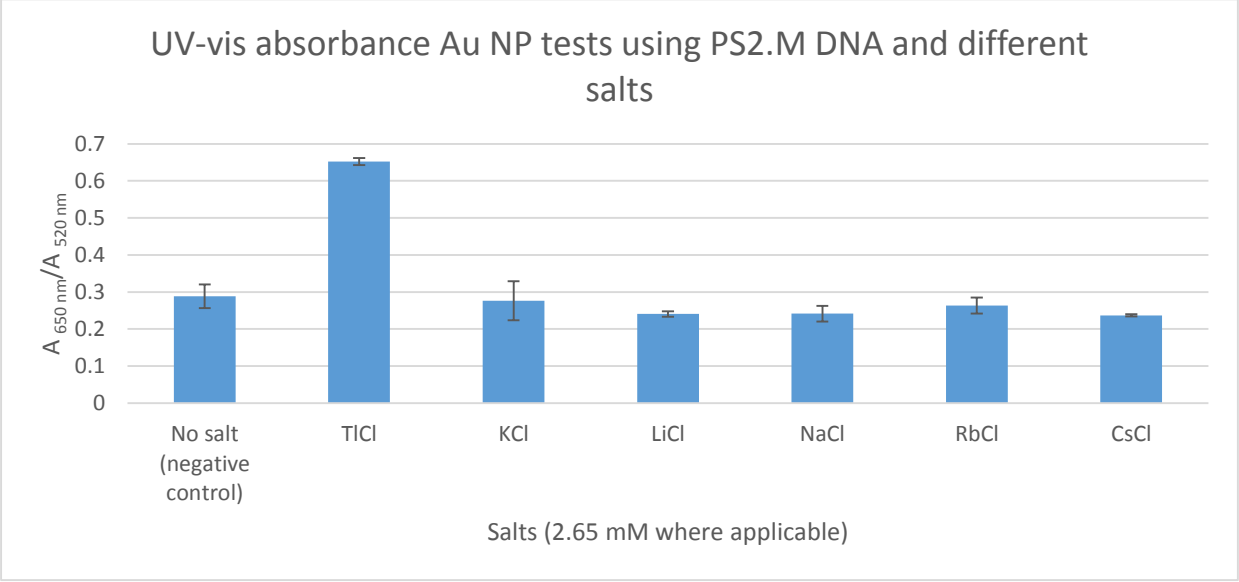

***Figure 26**: UV-vis absorbance tests for the Au NP colorimetric sensor system. From left to right: no salt (negative control), TlCl, KCl, LiCl, NaCl, RbCl, and CsCl. Data points were performed in triplicates.*

Sensitivity tests

Having demonstrated the selectivity of this sensor, the sensitivity of this system was tested next. Figure 27 is a photograph of the detection method under increasing concentrations of Tl^+ leads to a gradual progression of colour. This system could visually distinguish samples with concentrations as low as 10 µM Tl^+. Using UV-vis spectroscopy, the tested range of this system was approximately 1.3 - 165.6 µM Tl^+ (before adding Au NPs), and the linear range was found to be between 1.3 - 20 µM Tl^+. During these tests it became clear that the response plateaus at about 80 µM. The LOD for this system was calculated to be 4.56 µM Tl^+, at which point the signals begin to conflate with the other alkali metals. The sensitivity at the linear range appears to be 13.61 units/mM of Tl^+.

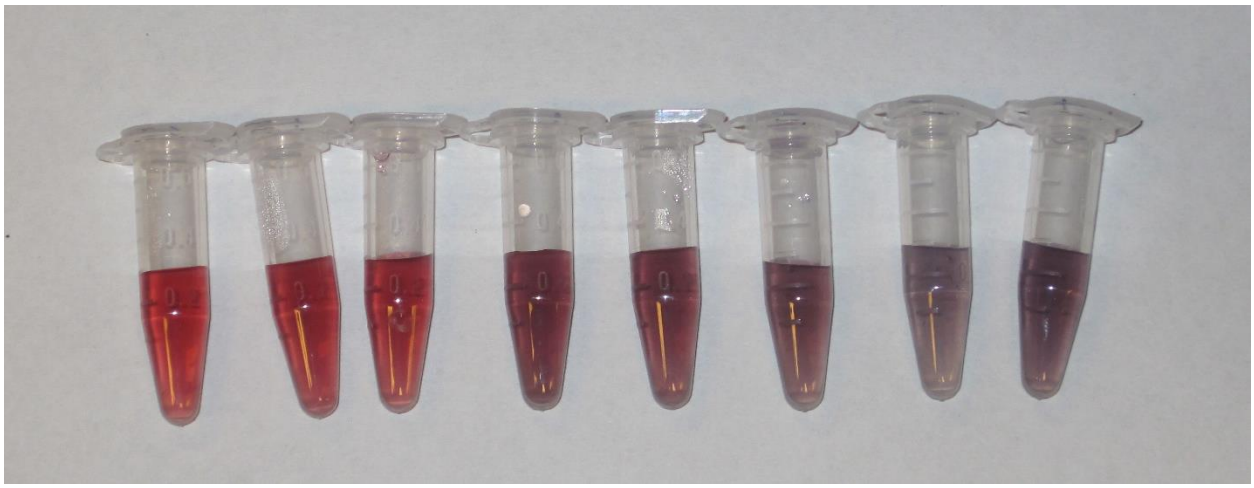

***Figure 27**: Tl^+ titration tests for the colorimetric Au NP PS2.M sensor. From left to right the Tl^+ concentrations were: 1.29 µM, 2.59 µM, 5.18 µM, 10.3 µM, 20.7 µM, 41.4 µM, 82.8 µM, 165.6 µM.*

As a control, the same experiment was repeated using the A15 (5′-AAAAAAAAAAAAAAA-3′) ssDNA sequence. This is to demonstrate the importance of the PS2.M aptamer for binding. The visual results showed that Tl^+ had little effect on the colour change in comparison to the PS2.M aptamer version (Figure 28). The UV-vis spectroscopy tests showed very little response towards

Tl^+ as well. Both of these results highly suggest that there is very little to no binding occurring between the A15 sequence and the analyte. This further suggests that the PS2.M aptamer selectively binds Tl^+ with a high affinity. These results are consistent with the mechanism outlined in Figure 23. Figure 29 is a graph comparing the absorbance response between the colorimetric experiments performed with PS2.M and A15 from the titration of TlCl. The linear range used to calculate the LOD, and sensitivity of the PS2.M system is displayed in Figure 30.

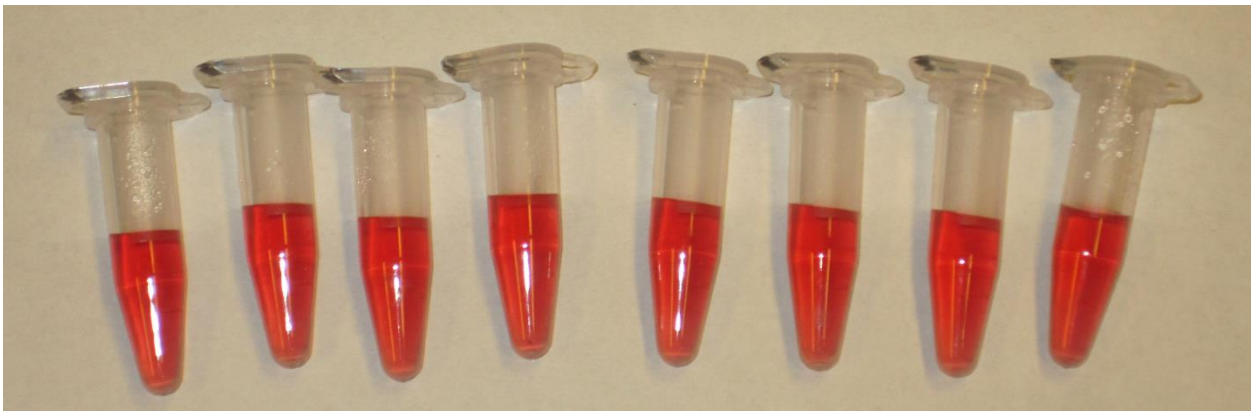

***Figure 28**: Tl^+ titration tests for the colorimetric Au NP A15 sensor. From left to right the Tl^+ concentrations were: 1.29 µM, 2.59 µM, 5.18 µM, 10.3 µM, 20.7 µM, 41.4 µM, 82.8 µM, 165.6 µM.*

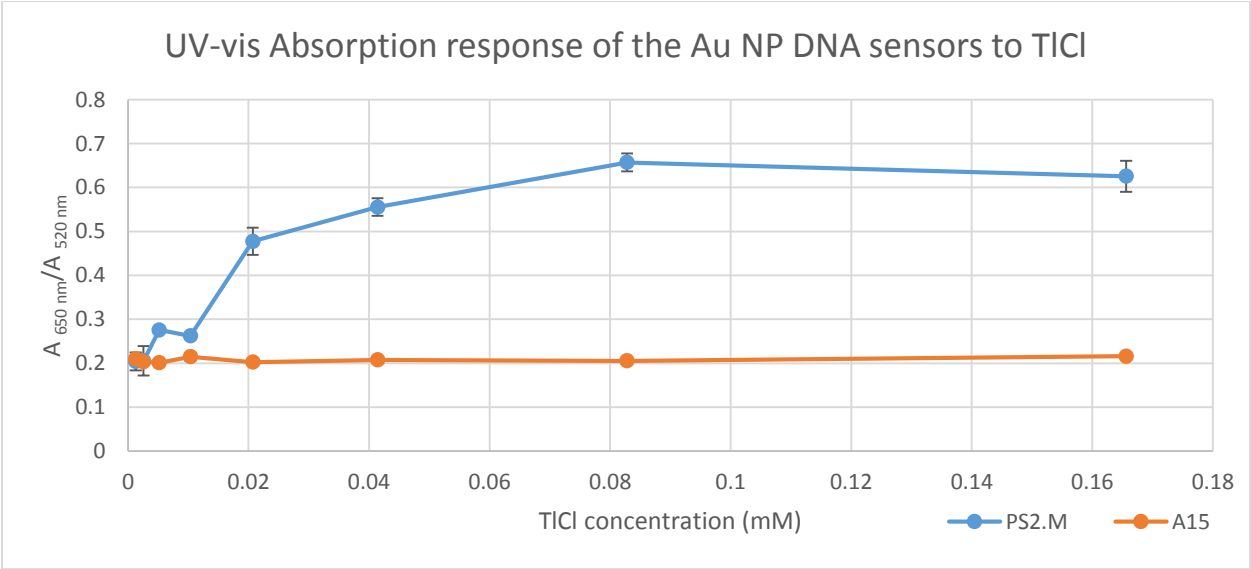

***Figure 29**: A Tl^+ titration comparison between using PS2.M, and A15 in the Au NP DNA sensor system. Data points performed in triplicate.*

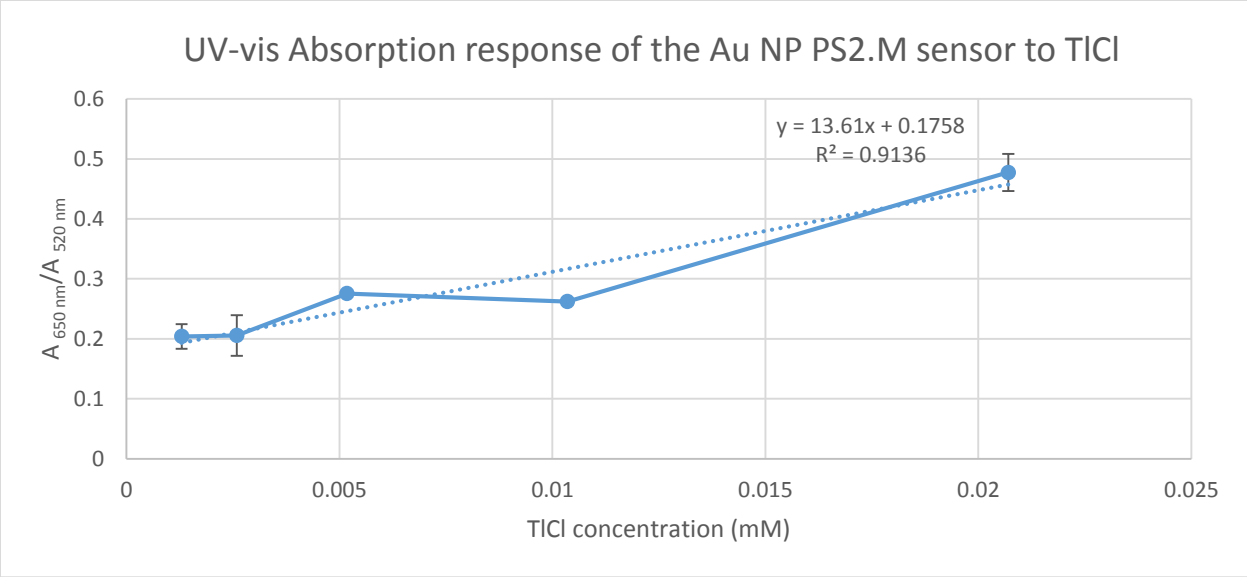

***Figure 30**: An inspection of the linear region for the PS2.M Au NP DNA sensor system for the detection of Tl^+. Data points performed in triplicates.*

Colorimetric tests without NaCl solution

Over the course of these titration tests it became apparent that even at concentrations as low as 2.65 mM Tl^+ is capable of producing Au NP aggregation after a few minutes. No NaCl is required for this colour change. This made it difficult to characterize the titration curve at concentrations over 165.6 µM because the curve would begin to dip and rise. At the time of this writing it is believed that at higher concentrations, the DNA isn't capable of complexing with most of the Tl^+ in solution anymore, which would allow for Tl^+ to interact with the Au NPs to cause aggregation. This is the most likely reason why the titration results past 165.6 µM (before adding the Au NPs) stops following the original trend (not shown).

This hypothesis was tested by performing the titration tests using increasing concentrations of Tl^+, without adding the 200 mM NaCl salt solution at the end. After several minutes the Au NP solutions with the highest concentrations of Tl^+ would show signs of aggregation through colour

change. The solution would eventually settle to the bottom of the vials overnight. These solutions were then analyzed under UV-vis absorption, which indicated that at concentrations of 165 μM and below (before adding the Au NPs) the Au NPs were unaffected by the presence of Tl^+. The UV-vis results also showed a higher level of discrimination between Tl^+ and other alkali ions. Figure 31 and Figure 32 display results of the sensitivity and selectivity tests performed, respectively.

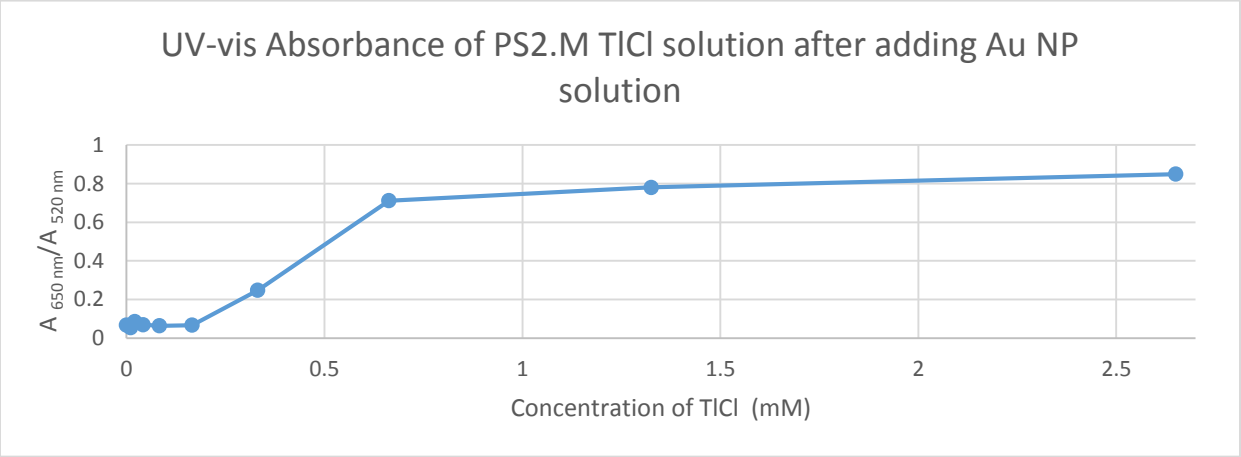

***Figure 31**: The colorimetric response of the PS2.M DNA Au NP detection system (without NaCl) to increasing concentrations of TlCl.*

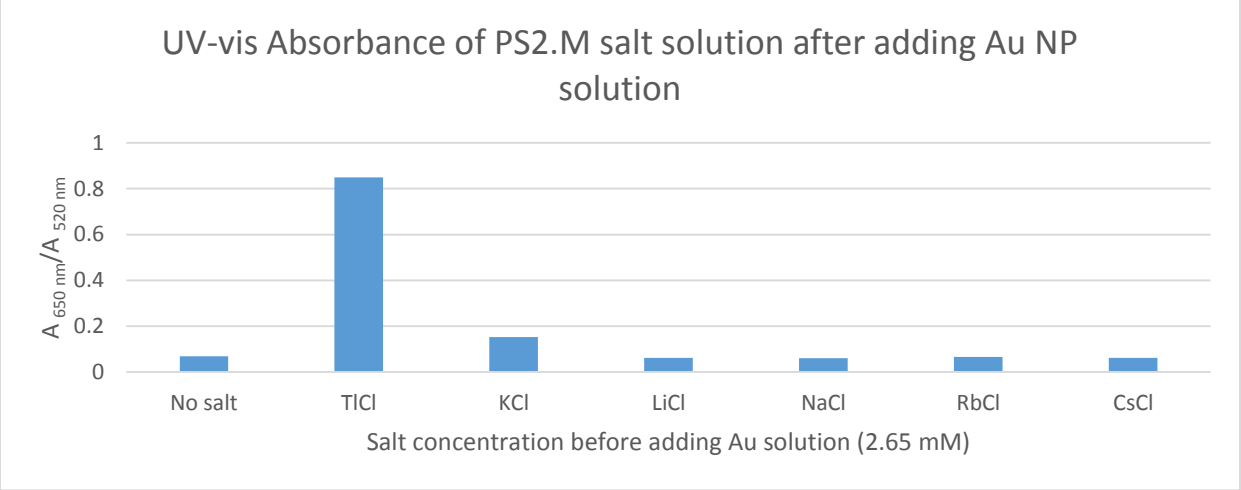

***Figure 32**: The colorimetric response of the PS2.M DNA Au NP detection system (without NaCl) to different metal ions.*

Materials and methods

The materials used for this section were as follows: ssDNA (PS2.M, and K^+-apt), Milli-Q water, 5 mM HEPES (pH 7.6), thallium chloride, lithium chloride, sodium chloride, potassium chloride, rubidium chloride, and caesium chloride. Also used were citrate capped Au NP solution (13 nm diameter, 13 nM), and 200 mM sodium chloride 5 mM HEPES (pH 7.6) buffer solution. All experiments were performed at room temperature. All analyte salts were dissolved into 13.25 mM (in 5 mM HEPES) stock solutions prior to starting the experiment. UV vis absorption analysis was done using the UV Agilent 8453 spectrophotometer instrument. All DNA was kept frozen until use.

Colorimetric tests

First, 3 µL of 100 µM DNA solution (dissolved in 5 mM HEPES buffer) is mixed with 3 µL of an analyte salt stock solution (concentration may vary), and 9 µL of 5 mM HEPES buffer is mixed together and left to sit for one minute. The second step comes from the addition of the Au NP solution (200 µL), finally the 200 mM sodium chloride 5 mM HEPES solution is added. Colour change should occur in under a minute. UV absorbance tests were performed using the 520 and 650 nm wavelengths. The final concentration of the DNA, analyte, Au NPs, and NaCl would be 1.1 µM, 0.12 mM, 8.25 nM, and 63.49 mM respectively. The photographs were taken on the same day, the samples were made.

Conclusions

Having determined the sensitivity and the selectivity of the PS2.M-FT aptamer, another attempt to demonstrate the applicability of the PS2.M aptamer in the form of the DNA Au NP based

colorimetric detection method was attempted. The colorimetric method has a lower LOD than using the FRET tests (4.56 µM, and 59.4 µM respectively). The colorimetric test also had a linear range between 1.3 - 20 µM (compared to 0 - 300 µM of the FRET based sensor). This method has a similar selectivity of Tl^+ over K^+, but a decreased selectivity for all of the other alkali metals to the FRET based sensor at the maximum tested concentration of Tl^+. The similarity in response of the negative control to the other non-potassium alkali metals suggests that there were very little to no interactions occurring with the PS2.M aptamer. This data corroborates with the FRET data, demonstrating the selectivity and sensitivity of the aptamer to Tl^+. The selectivity and sensitivity to Tl^+ indicates that the PS2.M is most likely binding to this ion.

We were able to show that the colorimetric sensor is able to produce a colour change even in the absence of the salt solution step at the end. Of the metal ions tested, only Tl^+ was able to produce a colour change without the sodium chloride solution addition at the final step. It is currently unclear how Tl^+ is interacting with the Au NPs to do this. It is suspected that at higher Tl^+ there aren't enough PS2.M aptamers to complex with the ion to prevent this aggregation, prior to the addition of the NaCl solution.

Chapter 4: Circular dichroism

The previous tests have displayed the binding affinity and selectivity of the PS2.M aptamer in detail. The described mechanisms for the detection methods used rely on aptamer-analyte structural conformational changes. These experiments lack a direct measurement of the aptamer structure after the addition of these metal ions. Of the methods available to measure the structural changes upon binding, circular dichroism (CD) was selected.

Circular dichroism: the mechanism of function

CD utilizes light made of two circularly polarized components.[106] The two components are of equal amplitudes. This technique exploits the properties of optically active chiral materials. In chiral materials, the refractive index for left (*laevo*) or right (*dextro*) circularly polarized light will be different, leading to different absorption values depending on the direction of the light. This effect manifests itself as positive or negative peaks on a spectrum.

The measurement of chirality for a molecule is determined by the differences in optical density for *laevo* and *dextro* circularly polarized light.[106] The measurements are performed as a function of wavelength, normally in the visible or ultraviolet bands.[106] The sensitivity to structure makes it useful for analysing changes in conformation for biomolecules.[107] CD measures the ellipticity to define the chirality of the molecules. In literature the units used to measure ellipticity are commonly defined as "degree cm^2/ dmol", "mdeg" or "L/ mol cm".[107,108] Ellipticity is directly correlated with absorption.[108] Figure 33 illustrates the principles and core concepts of this technique.

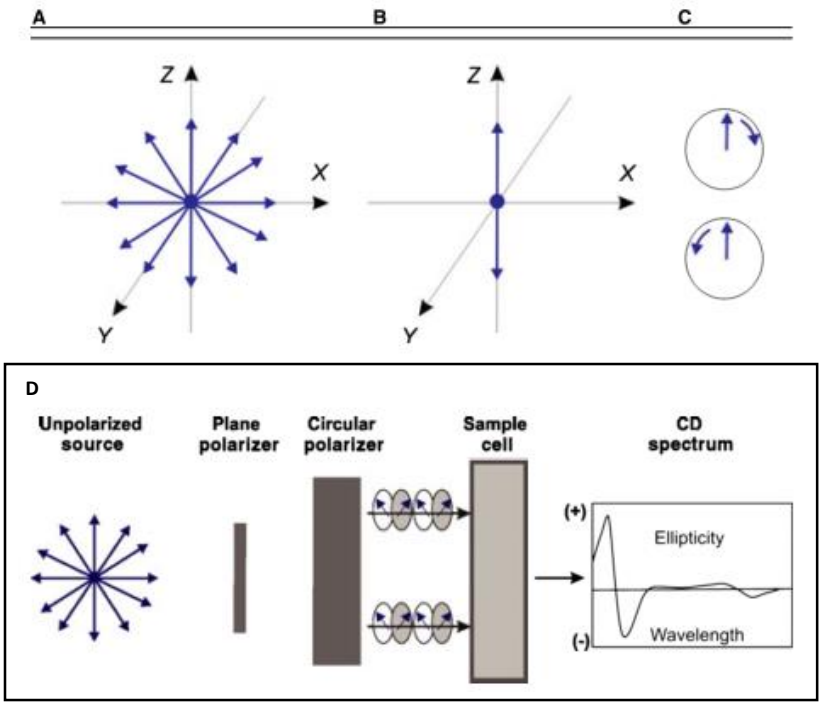

***Figure 33**: Schemes of the electric field components of unpolarised A), and polarized light B). For circularly polarized light C), it can move in a clockwise or counter clockwise direction. D) A diagram of how of CD measures a difference in absorption in chiral molecules. Reproduced from Ref 107 with permission of John Wiley and Sons.*

Circular dichroism: interpretation of data

DNA folding has been analysed under CD in various studies. CD measures the asymmetric backbone sugars in DNA, and their arrangements within the 3D structure.[109] Table 5 lists the three ways one may identify G-quadruplexes using CD. Positive peaks around 265 nm and negative peaks around 240 nm (group I) identify parallel structures. Anti-parallel structures may be identified by the positive peaks around 295 nm and 260 nm, with negative peaks at around 240 nm (group II).[109–113] Another form of the anti-parallel G-quadruplex may appear as positive peaks at around 295 nm and 240 nm, with a negative one at 260 nm (group III).[114,115]

Table 5*: A chart detailing the peaks necessary for the identification of G-quadruplex structures. Positive peaks are represented by "+" and negative peaks are represented by "-" .*[114,115]

Type	**~240 nm**	**~260 nm**	**~295 nm**
Parallel (group I)	+	-	N/A
Antiparallel (group II)	-	+	+
Antiparallel (group III)	+	-	+

The relationship between the G-quadruplex structure and wavelength absorbance was discovered using empirical evidence from other analysis techniques.[110] Limited theories currently exist that allow for the prediction of a CD spectrum from a structure or vice versa at the moment.[61] These differences may be due to the *syn* and *anti*-conformations of the glycosidic bonds found in the different G-quadruplex structures.[110,112] The base stacking geometry also affects the nature of the CD spectra as well.[110,112] The difference between group II and group III structures lie within the nature of their base stacking. Group III quadruplexes stack tetrads with consecutively distinct glycosidic bond angles on top of each other. Group II structures may stack identical and distinct glycosidic bond angles.[114] Every DNA sequence carries its own CD "signature" which is different from others.

Despite its widespread use in the characterization of DNA quadruplexes, scholars have noted that basing the structure of the aptamer solely on CD may be dangerous. In some cases the aptamers may bind using multiple conformations leading to spectrums that are unlike the ones mentioned above.[112] Though widely used, this technique still has not been developed to the point where the relationship between CD signatures and their structural attributes are fully understood.[110]

Rationale

CD is an important analytical technique for this project, because it provides a direct analysis of the aptamer-analyte structure. Earlier experiments could only obtain implicit data relating to structure from the changes in fluorescence signal, UV-vis absorption, or colorimetric change. By using CD, we could better understand the relationship between the G-rich aptamers and their resulting structures in the presence of Tl^+. The structural changes from the addition of ions could be further evidence for the proposed mechanisms for the detection methods described earlier. The selected concentrations of analyte salts were selected based on the results from the FRET experiments.

PS2.M CD results

Using Table 5 we can identify that the baseline spectrum (no analyte ions) is group III anti-parallel (positive peaks at 300 nm, and 240 nm, with a negative peak at 260 nm). The addition of K^+ and Tl^+ were able to show significant changes to the baseline CD spectrum. The resulting spectrums were different from each other, implying different structural properties from each other. This is no surprise given the FRET data, the colorimetric data, and how previous works have noted how this aptamer is more sensitive towards K^+ than other alkali metals.[113,116] The other alkali ions showed an insignificant change from the baseline CD spectrum in comparison.

While addition of K^+ and Tl^+ resulted in distinct CD spectrums from the baseline, it still presented group III anti-parallel peaks, similar to previous reports.[116,117] The addition of these ions increased the amplitude of the trend peaks for the identification of this structure. Tl^+ showed changes to the 300 nm and 260 nm peaks, while K^+ only increased the 300 nm peak. Other studies have reported a parallel structure for the PS2.M DNA.[118–120] In these cases K^+ was added in greater quantities than what was used in this project (>5 mM) which eventually increased the 260 nm peak and

decreased the peak at 300 nm, which would alter the structure from anti-parallel to parallel in their.[120] Figure 34 are the spectrums documenting our results. Given how Tl^+ and K^+ appeared to have altered the baseline spectrum the most, this would most likely indicate a cation stabilized structure.

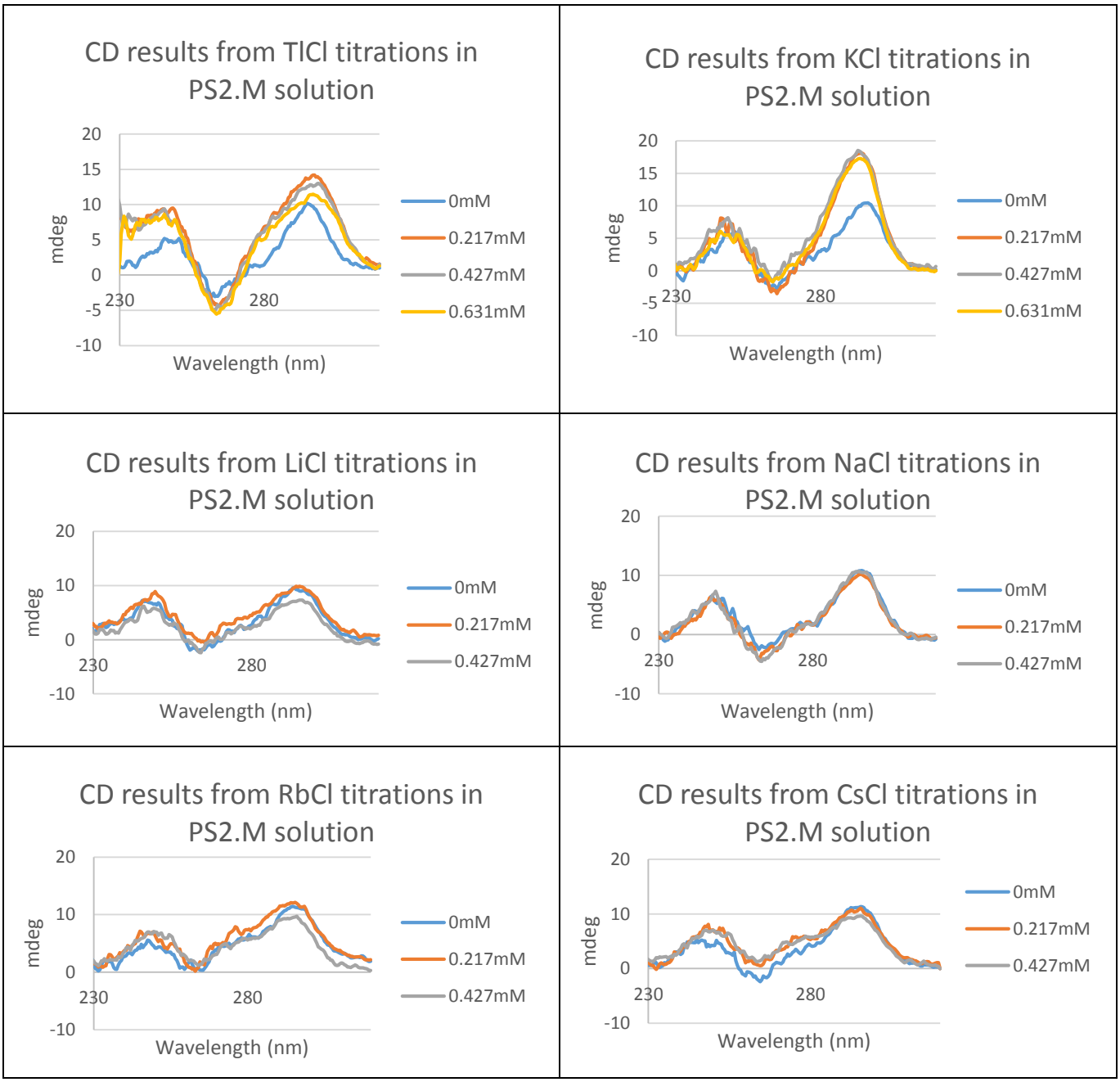

***Figure 34**: CD results from using PS2.M, with different salts at different concentrations. Buffer conditions 5 mM HEPES (pH 7.6) and 7.5 µM DNA.*

K^+-apt CD results

Studies using the K^+-apt aptamer have shown that the addition of K^+ displays a positive peak at ~295 nm and a negative one at ~233 nm, while Na^+ would have positive peaks at ~295 nm and a negative peak at ~260 nm.[121–123] Both would suggest (different kinds of) antiparallel structures. These results are similar to what was observed in this study.

As with PS2.M, the other alkali metals display lower amounts of structural change compared to Tl^+ and K^+. Tl^+ does not seem to clearly induce a G-quadruplex fold according to Table 5. The peak at 290 nm strongly indicates that antiparallel folding.[114,115] There may be many reasons for this. The first reason is that there may be a peak shift for the 230 nm peak to somewhere nearer to 200 nm, because a different ion was used. Phenomena like this have been reported before.[116] The second reason may be because there are several different G-quadruplex structures co-existing at the same time. The superposition of all these different spectra would make interpretation difficult. We could not document wavelengths much lower than 230 nm because increasing Tl^+ concentrations causes interference with the readings at those wavelengths. Figure 35 documents the spectra obtained from this experiment.

It was difficult to say if there were any significant changes in structure from the addition of the other alkali metals tested, as the peak changes were minimal suggesting that these ions did not change the original structure of the aptamer in solution (anti-parallel, group III). It is almost certain that Tl^+ and K^+ did. Of these two it is almost certain that K^+ induced a G-quadruplex conformational change (anti-parallel, group II).

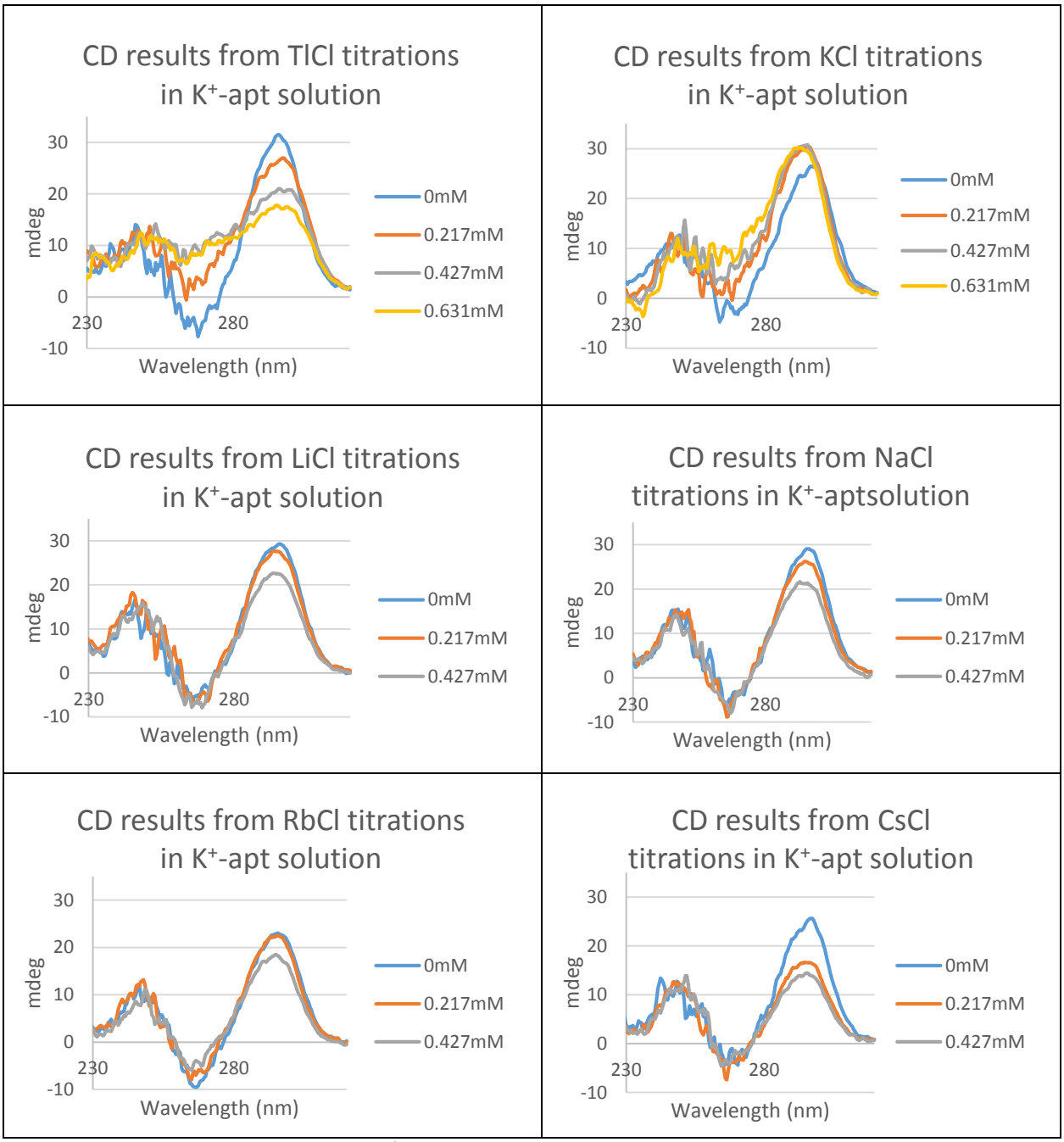

***Figure 35**: CD results from using the K^+-apt aptamer, with different salts at different concentrations. Buffer conditions 5 mM HEPES (pH 7.6) and 7.5 µM DNA.*

Materials and methods

The materials used for this section were as follows: ssDNA (PS2.M, and K^+-apt), Milli-Q water, 5 mM HEPES (pH 7.6), thallium chloride, lithium chloride, sodium chloride, potassium chloride, rubidium chloride, and caesium chloride. All experiments were performed at 20^0 C in 5 mM HEPES. All salts were dissolved to a concentration of 13.25 mM in 5 mM HEPES prior to starting the experiment. All DNA was kept frozen until use.

CD measurements

200 µL of a 7.5 µM DNA aptamer solution (dissolved in a 5 mM HEPES (pH 7.6) buffer) would be added to a UV-vis cuvette with a path length of 1 cm. Titration experiments were done by adding identical amounts of salt analyte solution (using the stock) to the DNA solution in the cuvette. In order to account for the effects of buffer on the CD readings, the ellipticity of three blank buffer solutions were measured and averaged. Subsequent titration experiment readings would be subtracted by the blank buffer data. All measurements were performed on the Jasco J-715 Spectrophotometer.

Measurements on the CD instrument were performed using a continuous scanning mode (100 nm/min) from 230 nm to 330 nm, with a sensitivity of 100 mdeg. Other settings include a 0.5 nm data pitch, 1-second response, 1.0 nm bandwidth. The measurements made were the average of three scans per sample.

Conclusions

From the data gathered here, it would seem that the K^+ and Tl^+ ions induce structural changes in the aptamers, while the other ions had a negligible response. The CD results for the PS2.M aptamer showed a baseline spectrum with positive peaks at around 300 nm, 240 nm, and a negative peak at 260 nm. These are distinct markers for the antiparallel G-quadruplex structure (group III). The increase of K^+ and Tl^+ ion concentrations, lead to a significant change in their CD spectrum. These distinct new spectrums were still identified as antiparallel (group III), however the addition of these ions increased the amplitude of the trend peaks required for the identification for this structure. This would suggest an induced structural change. The difference in peak signatures indicate different, although similar structures. This corroborates with the information obtained from the fluorescence spectrum data.

Since the peaks were there before adding the analytes, this might have to do with the Na^+ already in the buffer. This would allow for a mixture of G-quadruplex and random conformations (which would have no distinct CD peaks) with the CD spectrum being a superposition of these different structures. The addition of Tl^+ and K^+ most likely shifted the equilibrium more towards the G-quadruplex structure. The different affinities for different ions, the different properties of each ion, and shifting equilibriums may also explain why only the 518 nm peak in the fluorescence spectrum data dropped when using K^+.

The change in structure for the K^+-apt aptamer was prominent. The original baseline spectrum could be identified as an antiparallel structure (group III). Following the addition of K^+ and Tl^+, the peaks seem to indicate a group II structure, through the increase of the 260 nm peak, and a

decrease in the 230 nm peak. While K^+ and Tl^+ displays an obvious change from the original baseline, only K^+ produced peaks that could be unequivocally identified as group II. The altered spectrum from Tl^+ appeared to be missing a required peak necessary for group II identification. It is unclear at this moment whether the interactions with Tl^+ result in the formation other structures, if the negative peak shifted nearer to the 200 nm region, or if the peaks are simply a super position of several different structures.

Chapter 5: Isothermal titration calorimetry

Isothermal titration calorimetry (ITC) is a technique used to measure the enthalpy of a reaction. The process of binding give rise to exothermic or endothermic effects.[69] Utilizing this process, one is able to probe into the fundamental forces driving a reaction. Thus, by using this technique, it would be possible to confirm that detection methods used earlier, were a result of the analyte ions binding with the aptamer.

Isothermal titration calorimetry: mechanism and function

The basic designs for isothermal titration calorimetry utilizes two cells, with one acting as a reference (containing only water) , and the other acting as the sample cell.[124] The sample cell is filled with a solution containing one component of the complex (i.e. an aptamer). Prior to starting the experiment an injector would be filled with the other half of the complex (i.e. the ionic solution).[69] The injector would be placed inside the sample cell, from there the system would be given time to equilibrate to a set temperature before beginning the experiment.[124] Once the experiment begins, the injector typically also acts as a stirrer, and begins to inject identical amounts of solution over a regular interval. The reaction between the two components of the complex would cause a change in enthalpy. The system measures this heat change compared to the reference cell. These measurements are used to calculate meaningful data regarding the system.[124] Typically a blank experiment where the binding component in the sample cell is not used will be performed. This is to correct for the enthalpy effects from dilution from the experimental data.[125] This is typically done before the final calculations characterizing the binding reaction is performed.[125]

At the end of the reaction, several values are calculated to provide greater insight into the system. Values often obtained after the binding reaction are the binding constant (K_b), enthalpy of binding ($\Delta H°$), and the number of binding sites (*n*).[125] These values are derived from two graphs produced during the binding experiments: the raw ITC data, and the integrated heat data.[125,126] The raw ITC data compares the thermal power (µcal/s) over the time for each injection, and the integrated heat data compares the thermal power to the molar ratio of the injected ligand to the binding molecule present in the sample cell. The integrated heat data is calculated from the heat data using the known molar concentrations in the injectant and sample cell prior to the experiment.[125]

Rationale

Previous experiments using FRET, colorimetric, absorption methods highlighted the sensory properties of the PS2.M aptamer. Using CD we were able to confirm that K^+ and Tl^+ induced significant structural changes in the DNA aptamers tested. ITC is used to provide a more direct measure of binding. As mentioned before, if binding occurs there should be a change in enthalpy. The information provided from this method would be able to confirm that the results from the earlier tests were caused by aptamer binding.

ITC results

The following data uses ionic solutions (0.828 mM) injected into a sample cell of 40 µM DNA. In both cases a buffer solution of 5 mM HEPES (pH 7.6) was used as the solvent. The blank background data was measured by injecting the ionic solution into a blank buffer solution (no DNA). Previous studies have determined that the stabilizing effects of alkali metals on G-quadruplexes were ordered in the following manner: $K^+ >> Na^+ > Rb^+ > NH_4^+ > Cs^+ >> Li^+$.[69] For the

most part, the binding enthalpy data appears to agree with this trend. For these tests Tl^+, K^+, and Li^+ were tested against the DNA strand PS2.M.

The values of *n* were not calculated for this experiment; instead, the values were selected from a previous work that had already attempted to define the number of binding sites of an ion to an aptamer. For PS2.M the number of sites for K^+, and Na^+ were one, and three respectively.[116] Given the noted similarities between K^+ and Tl^+, Tl^+ used the same *n* values for as K^+ wherever possible.

The amount of heat released from the aptamer-binding experiments was quite low. These tests showed that Tl^+ produced the largest enthalpy changes out of all the ions tested. This reaffirmed the results from earlier, as thallium always produced the largest response. These results combined with the earlier data strongly indicate that Tl^+ binds with the PS2.M aptamer. K^+ was shown to have lower levels of heat change. In comparison, Li^+ displayed lower, to negligible levels of binding enthalpy. Figure 36 documents our results.

From the data presented, we see that the integrated Tl^+ data has a strong enough trend to fit a reasonable curve, whereas K^+ cannot. From the raw ITC data, we see the kinetics for K^+ is generally faster than the kinetics for Tl^+. The sharp heat release indicates a quick return to equilibrium, whereas the curves for Tl^+ took longer to reach equilibrium. These results are consistent with the fluorescence based kinetics data observed earlier.

TlCl

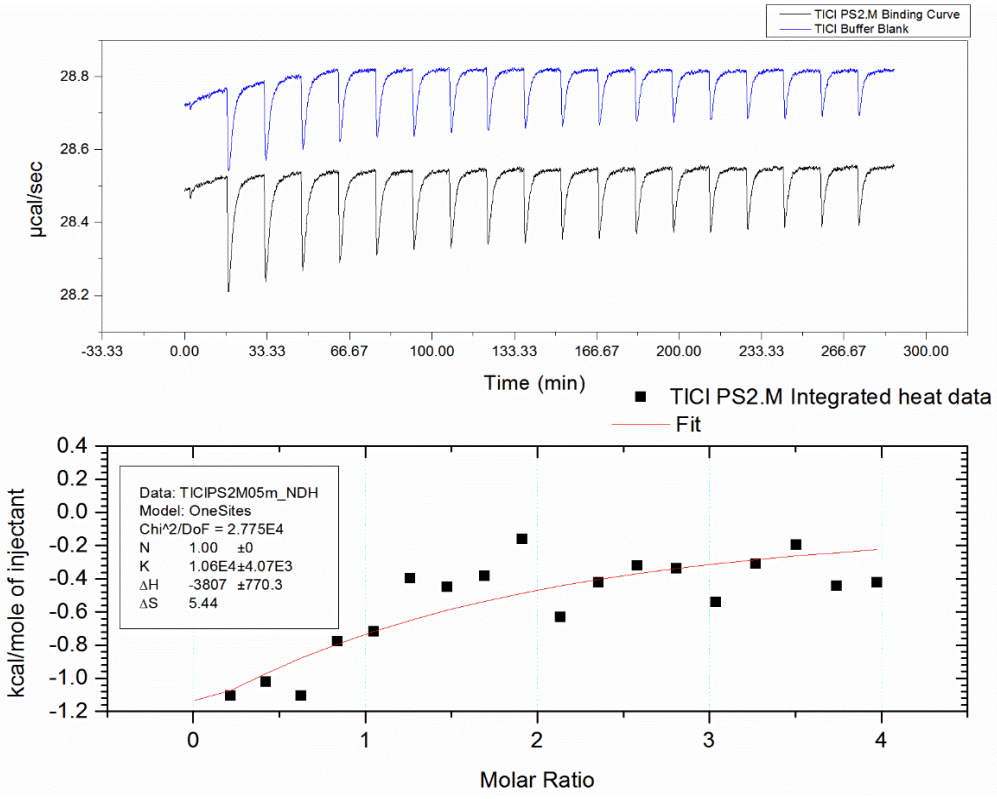
TlCl PS2.M Binding Curve
TlCl Buffer Blank
µcal/sec
Time (min)
TlCl PS2.M Integrated heat data
Fit
Data: TlClPS2M05m_NDH
Model: OneSites
Chi^2/DoF = 2.775E4
N 1.00 ±0
K 1.06E4±4.07E3
ΔH -3807 ±770.3
ΔS 5.44
kcal/mole of injectant
Molar Ratio

KCl

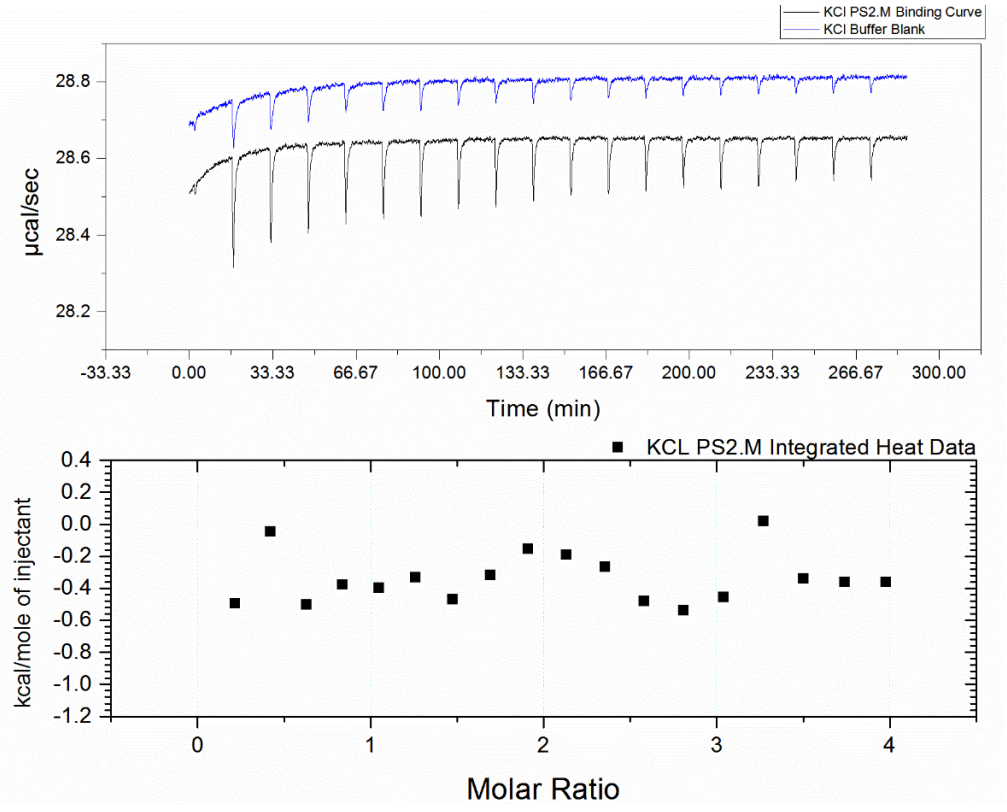
KCl PS2.M Binding Curve
KCl Buffer Blank
µcal/sec
Time (min)
KCL PS2.M Integrated Heat Data
kcal/mole of injectant
Molar Ratio

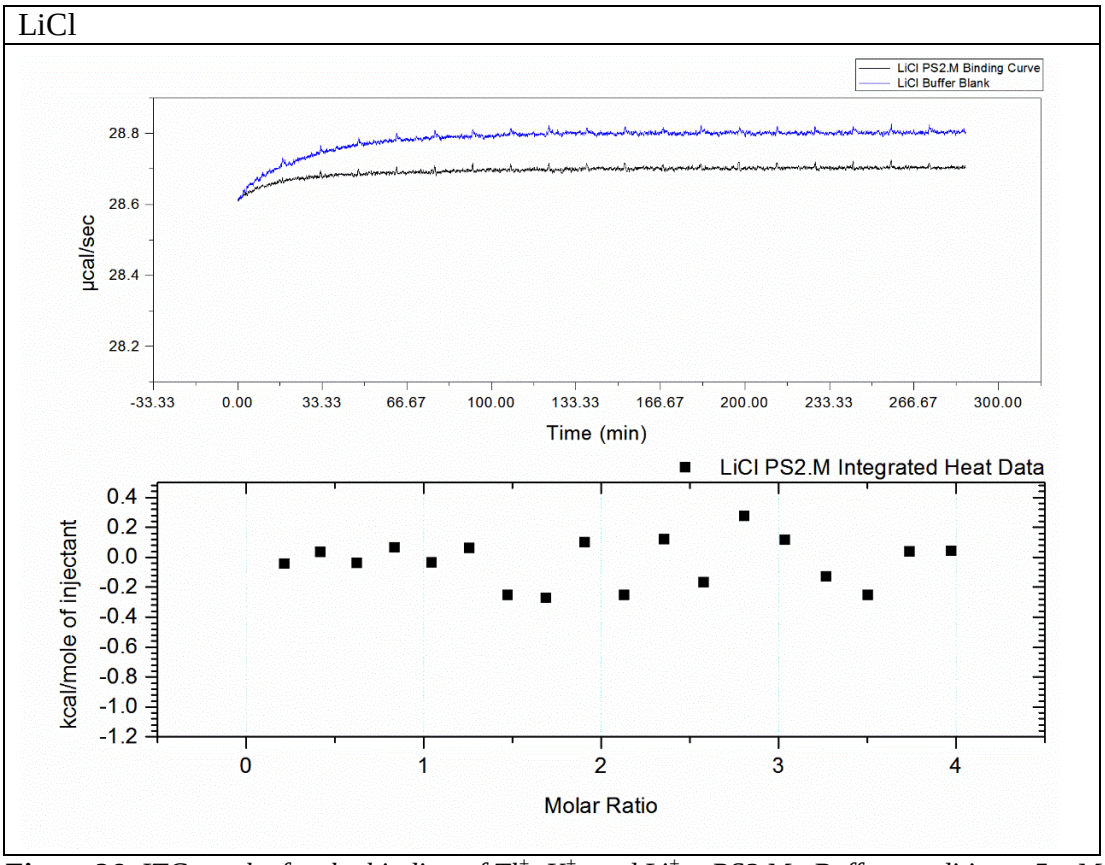

***Figure 36**: ITC results for the binding of Tl^+, K^+, and Li^+ to PS2.M.. Buffer conditions: 5 mM HEPES (pH 7.6), 40 µM DNA.*

Materials and methods

The materials used for this section were as follows: ssDNA (PS2.M), Milli-Q water, 5 mM HEPES (pH 7.6), thallium chloride, lithium chloride, and potassium chloride. All experiments were performed at 20^0 C in 5 mM HEPES. All analyte salts were dissolved to a concentration of 0.828 mM in 5 mM HEPES prior to starting the experiment. All DNA was kept frozen until use. Calorimetry experiments were performed on the MicroCal VPT-ITC microcalorimeter. The experiments were performed with 19 injections in total, using a reference power of 30 µCal/sec.

Methods

The binding experiments were performed as follows; the sample cell would be filled with 1.445 mL 5 mM HEPES solution with 40 µM DNA. Once the binding experiment began 1 µL of analyte salt solution would be injected after 200 seconds, then 15 µL after every 900 seconds thereafter. This would continue until 271 µL of the injectant is used up. The same experiment would be performed again without the DNA to be used as the blank experiment. The obtained data would be subtracted by the blank data to correct for dilution effects.

Conclusions

From these experiments it would appear that the enthalpy changes produced were low, with Tl^+ having the highest enthalpy change amongst all of the ions tested, and K^+ coming in second. The other ion, Li^+ displayed negligible response. The trend of these results is comparable to what was observed in earlier sections. Given these results it would be safe to conclude that Tl^+ induces the most binding. The raw ITC graphs also show a slower recovery rate to Tl^+, this is consistent with the binding kinetics observed in chapter 2.

Chapter 6: Conclusions and future work

From the data presented, we showed that of the G-quadruplex forming DNA aptamers studied, PS2.M was the most sensitive towards Tl^+, followed by the K^+-apt. The FRET titration data showed that PS2.M was more selective than K^+ apt, and thus became the aptamer of focus for this thesis. Starting from here, we demonstrated the Tl^+ sensory applications of the PS2.M.

For this project, two different detection methods were utilized: the FRET based aptamer sensor, and the colorimetric based sensor. Both sensors displayed a high level of discrimination against the similar alkali metal ions. The FRET based sensor was also able to detect Tl^+ in the presence of other alkali metals. This would indicate the stronger binding of Tl^+ to the PS2.M aptamer over the other ions. The sensor displayed a dynamic range of ~1 mM Tl^+, a linear range of up to 300 µM Tl^+, a sensitivity of 2.48 units/ mM Tl^+, and a LOD of 59 µM Tl^+. The FRET based sensor was also able to detect spiked Tl^+ in Lake Ontario water. Under these conditions a linear range of 0 - 1.5 mM Tl^+, a sensitivity of 0.245 units/ mM Tl^+ and a LOD of 0.27 mM Tl^+ was observed. Other observed phenomena include the different ways Tl^+ and K^+ induced fluorescence spectrum changes to the PS2.M-FT aptamer possibly indicating different conformer formations, and the slower binding kinetics of Tl^+ to the PS2.M-FT aptamer. The slower kinetics might be due to the tighter binding of thallium ions to haildes.

Since the FRET based system requires expensive dye labelling, and instrumental analysis, a colorimetric detection method was attempted. The colorimetric sensor appears to have a dynamic range of 1.3 - 80 µM Tl^+, with a linear range of 1.3 - 20 µM Tl^+, a sensitivity of 13.61 units/mM

of Tl^+ and a LOD of 4.56 µM Tl^+. Tl^+ induced colour changes were readily observable to the naked eye at concentrations as low as 10 µM. The two sensors displayed different linear ranges and LODs despite the use of the same aptamer. As a further test of the importance of the PS2.M DNA in Tl^+ sensing, the sensor was tested again to detect Tl^+ using the negative control A15 DNA strand. These results demonstrated the importance of the PS2.M aptamer's selectivity and affinity to Tl^+ for detection applications. Given these results, these sensors may be useful for real world sensory applications in the real world.

As explained earlier, the sensor's mechanism relies on the conformational changes of the aptamers when binding towards the target. In this case, the structure in question was hypothesized as the G-quadruplex. One earlier report has already indicated that Tl^+ and K^+ were able to produce similar G-quadruplex structures with one particular strand of aptamer. The results from this project strongly indicate that Tl^+ and K^+ bind to aptamers to form G-quadruplexes. As noted before, the FRET signal was highest when binding experiments were performed using these two ions. The FRET signals are inversely correlated to the distance between the dyes on each end of the aptamer, which would suggest a structural change occurred. The higher FRET signal from Tl^+ implies that the resulting G-quadruplex structure was tighter than the K^+ derived conformation. Since flexible unbound ssDNA can adsorb on the surface of Au NPs, Au NP aggregation in the presence of Tl^+ indicates aptamer binding to the target, preventing adsorption. In order to further prove that these sensors work as hypothesized, further tests using CD, and ITC were performed to analyse the structure, and binding directly.

The CD results showed that the addition of the Tl^+ and K^+ ions produced the largest amount of change in the CD spectrum, indicating that the original aptamer conformation (with no analyte) was altered by their presence. With the PS2.M aptamer, it became apparent that the presence of these two ions induced an altered form of the anti-parallel (group III) that was very different from the baseline spectrum. The Tl^+ and K^+ induced spectrums were different from each other, implying different structural properties from each other. This conforms to the data found for the fluorescence spectra for PS2.M-FT. These two ions also produced the largest changes to the baseline K^+-apt aptamer CD spectrum as well (group III, antiparallel). K^+ induced what appeared to be an anti-parallel (group II) structure. Tl^+ also produced similar peak intensity shifts; however, the CD signature could not be clearly interpreted as any known structure. The spectrum was missing the required negative peak (~240 nm), for group II identification. Presently there are two theories to explain this. The first reason is that the negative peak shifted further to the left, leaving it undetected. The second reason is that the CD signature is actually a super position of many structures, making analysis difficult. The peak at 295 nm suggests an antiparallel structure.[114,115]

The ITC experiments demonstrated that Tl^+ and K^+ binding have the highest change in enthalpy out of all the other ions in the experiments performed with PS2.M. This would indicate that binding is occurring during the previous experiments. Of the ions tested only Tl^+ showed a strong enough trend to fit a binding curve. The other ion, Li^+ was used as a control showed negligible response. This is reasonable as it follows the same pattern reported in previous literature. The raw ITC data showed that Tl^+ had slower kinetics than K^+, similar to the data found in using the FRET aptamers.

Given the CD, and ITC results it would be safe to say that Tl^+ is most likely binding to the PS2.M aptamer to form a G-quadruplex. This would mean that the mechanism proposed for the detection methods mentioned earlier are most likely true. In summary, a highly selective probe for Tl^+ was identified in this thesis work. Its application in making biosensors and its fundamental binding interactions with Tl+ have been studied.

Future work

The work presented here has only detailed Tl^+ detection using G-quadruplex forming DNA. While this was successful it provided very little information regarding the relationship between Tl^+ and K^+ binding to aptamers. The majority of this thesis focused on the PS2.M aptamer. More DNA strands need to be tested before a comprehensive understanding regarding the trends between these ions and aptamer binding may be obtained. Of the methods described the FRET based sensor is very useful in obtaining information quickly, and should be pursued further to develop a highly sensitive and selective biosensor for Tl^+. The FRET based method, could be used to measure, selectivity, sensitivity, and binding kinetics.

Structural information from CD may be inadequate at times as the information obtained is not always be reliable. Other papers have named NMR and X-ray crystallography as more detailed characterization methods for studying the structure. This may be useful in studying the structural changes of the K^+-apt aptamer due to Tl^+.

Bibliography

1. Gadd, G. M. & Griffiths, A. J. Microorganisms and Heavy Metal Toxicity. *Microb. Ecol.* **4,** 303–317 (1978).

2. Giller, K. E. N. E., Witter, E. & Mcgrath, S. P. TOXICITY OF HEAVY METALS TO MICROORGANISMS AND MICROBIAL PROCESSES IN AGRICULTURAL SOILS : A REVIEW. *Soil Biol. Biochem.* **30,** 1389–1414 (1998).

3. Duruibe, J. O., Ogwuegbu, M. O. C. & Egwurugwu, J. N. Heavy metal pollution and human biotoxic effects. *Int. J. Phys. Sci.* **2,** 112–118 (2007).

4. Wang, Y. *et al.* The influence of soil heavy metals pollution on soil microbial biomass, enzyme activity, and community composition near a copper smelter. *Ecotoxicol. Environ. Saf.* **67,** 75–81 (2007).

5. Cheng, S. Heavy Metal Pollution in China : Origin , Pattern and Control. *Environ. Sci. Pollut. Res.* **10,** 192–198 (2003).

6. Jarup, L. Hazards of heavy metal contamination. *Br. Med. Bull.* **68,** 167–182 (2003).

7. Babel, S. & Kurniawan, T. A. Low-cost adsorbents for heavy metals uptake from contaminated water : a review. *J. Hazard. Mater.* **97,** 219–243 (2003).

8. Peter, A. L. J. & Viraraghavan, T. Thallium: a review of public health and environmental concerns. *Environ. Int.* **31,** 493–501 (2005).

9. Martín, F. *et al.* Thallium Behavior in Soils Polluted by Pyrite Tailings (Aznalcóllar, Spain). *Soil Sediment Contam. An Int. J.* **13,** 25–36 (2010).

10. Li, S., Huang, W., Duan, Y., Xing, J. & Zhou, Y. Human fatality due to thallium poisoning: autopsy, microscopy, and mass spectrometry assays. *J. Forensic Sci.* **60,** 247–51 (2015).

11. Tsai, Y.-T. *et al.* Central nervous system effects in acute thallium poisoning. *Neurotoxicology* **27,** 291–295 (2006).

12. Bank, W. J., Pleasure, D. E., Suzuki, K. & Nigro, M. Thallium Poisoning. *Arch Neurol* **26,** 456 – 464 (2015).

13. Galva, S. & Santamarı, A. Thallium toxicity. *Toxicol. Lett.* **99,** 1–13 (1998).

14. Kazantzis, G. Thallium in the environment and health effects. *Enviromental Geochemistry Heal.* **22,** 275–280 (2000).

15. Zitko, V. TOXCITY AND POLLUTION POTENTIAL OF THALLIUM. *Sci. Total Environ.* **4,** 185–192 (1975).

16. LaCoste, C., Robinson, B. & Brooks, R. Uptake of Thallium By Vegetables: Its Significance for Human Health, Phytoremediation, and Phytomining. *J. Plant Nutr.* **24,** 1205–1215 (2001).

17. Xiao, T. *et al.* Naturally occurring thallium: a hidden geoenvironmental health hazard? *Environ. Int.* **30,** 501–507 (2004).

18. Madejon, P. in *Heavy Met. Soils Trace Met. Met. Soils their Bioavailab.* (Alloway, B. J.) **22,** 543–549 (Springer Netherlands, 2013).

19. Dmowski, K., Rossa, M., Kowalska, J. & Krasnodębska-Ostręga, B. Thallium in spawn, juveniles, and adult common toads (Bufo bufo) living in the vicinity of a zinc-mining complex, Poland. *Environ. Monit. Assess.* **187,** 4140–4147 (2015).

20. Wierzbicka, M., Szarek-Łukaszewska, G. & Grodzińska, K. Highly toxic thallium in plants from the vicinity of Olkusz (Poland). *Ecotoxicol. Environ. Saf.* **59,** 84–88 (2004).

21. Poletti, J., Pozebon, D., de Fraga, M. V. B., Dressler, V. L. & de Moraes, D. P. Toxic and micronutrient elements in organic, brown and polished rice in Brazil. *Food Addit. Contam. Part B, Surveill.* **7,** 63–69 (2014).

22. Douglas, K. T., Bunn, M. A. & Baindur, S. R. THALLIUM IN BIOCHEMISTRY. *Int. J. Biochem.* **22,** 429–438 (1990).

23. Housecroft, C. E. & Sharpe, A. G. *Inorganic Chemistry*. 18, 297, 875–876, & 880–883 (Prentice Hall, 2004).

24. Lee, A. G. The Coordination Chemistry of Thallium(I). *Coord. Chem. Rev.* **8,** 289– 349 (1972).

25. Sabbioni, E., Goetz, L., Marafante, E., Gegotti, C. & Manzo, L. Metabolic fate of different inorganic and organic species of thallium in the rat. *Sci. Total Environ.* **15,** 123–135 (1980).

26. Nakano, J. On some Potassium-Like Qualities of the Thallium Ion. *Specialia* **759,** 1967–1968 (1968).

27. Tao, Z., Gameiro, A. & Grewer, C. Thallium Ions Can Replace both Sodium and Potassium Ions in the Glutamate Transporter Excitatory Amino Acid Carrier 1 †. *Biochemistry* **47,** 12923–12930 (2008).

28. Hoffman, R. S. Thallium Toxicity and the Role of Prussian Blue in Therapy. *Toxicol Rev* **22,** 29–40 (2003).

29. Labianca, D. A. A Classic Case of Thallium Poisoning and Scientific Serendipity. *J. Chem. Educ.* **67,** 1019–1021 (1990).

30. Ammann, A. A. SPECIAL FEATURE : Inductively coupled plasma mass spectrometry (ICP MS): a versatile tool. *J. Mass Spectrom.* **42,** 419–427 (2007).

31. Thomas, R. TUTORIAL A Beginner ' s Guide to ICP-MS. *Spectroscopy* **16,** 38–55 (2001).

32. Mcconnell, J. R. & Edwards, R. Coal burning leaves toxic heavy metal legacy in the Arctic. *Proc. Natl. Acad. Sci.* **105,** 12140–12144 (2008).

33. Medek, P., Pavlíčková, J., Zbíral, J., Čižmárová, E. & Kubáň, V. Inductively Coupled Plasma Mass Spectrometric (ICP/MS) Determination of Thallium in Soils and Winter Rapeseeds. *Int. J. Environ. Anal. Chem.* **81,** 207–219 (2001).

34. Zbiral, J., Medek, P., Kubán, V., Čižmárová, E. & Němec, P. Analytical methods and quality assurance. *Commun. Soil Sci. Plant Anal.* **31,** 2045–2051 (2000).

35. Böning, P. & Schnetger, B. Rapid and accurate determination of thallium in seawater using SF-ICP-MS. *Talanta* **85,** 1695–1697 (2011).

36. Robinson, J. W. & Rouge, B. Atomic Absorption Spectroscopy. *Anal. Chem.* **32,** 17 A–29 A (1960).

37. Piccolo, B. & Connor, R. T. O. Atomic Absorption Spectroscopy '. *J. Am. Oil Chem. Soc.* **45,** 789–792 (1968).

38. Xiao-quan, S., Zhe-ming, N. I. & Li, Z. APPLICATON OF MATRIX MODIFICATION IN DETERMINATIO OF THALLIUM IN WASTE WATER BY GRAPHITE-FURNACE ATOMIC-ABSORPTION SPECTROMETRY. **31,** 150–152 (1984).

39. Silva, A. F. *et al.* Method development for the determination of thallium in coal using solid sampling graphite furnace atomic absorption spectrometry with continuum source, high-resolution monochromator and CCD array detector. *Spectrochim. Acta Part B At. Spectrosc.* **59,** 841–850 (2004).

40. Sturgeon, E., Chakrabarti, C. L. & Langford, C. H. Studies on the Mechanism of Atom Formation in Graphite Furnace Atomic Absorption Spectrometry. *Anal. Chem.* **48,** 1792–1807 (1976).

41. Cheraghi, S., Taher, M. A. & Fazelirad, H. Voltammetric sensing of thallium at a carbon paste electrode modified with a crown ether. *Microchim. Acta* **180,** 1157–1163 (2013).

42. Kokkinos, C., Raptis, I., Economou, A. & Speliotis, T. Determination of Trace Tl(I) by Anodic Stripping Voltammetry on Novel Disposable Microfabricated Bismuth-Film Sensors. *Electroanalysis* **22,** 2359–2365 (2010).

43. Ermolenko, Y. *et al.* New membrane material for thallium (I)-selective sensors based on arsenic sulfide glasses. *Sensors Actuators B Chem.* **207,** 940–944 (2015).

44. Ibupoto, Z. H., Ali, S. M. U., Khun, K. & Willander, M. Selective Thallium (I) Ion Sensor Based on Functionalised ZnO Nanorods. *J. Nanotechnol.* **2012,** 1–6 (2012).

45. Perrault, J. R., Buchweitz, J. P. & Lehner, A. F. Essential, trace and toxic element concentrations in the liver of the world's largest bony fish, the ocean sunfish (Mola mola). *Mar. Pollut. Bull.* **79,** 348–353 (2014).

46. Chamsaz, M., Arbab-Zavar, M. H., Darroudi, A. & Salehi, T. Preconcentration of thallium (I) by single drop microextraction with electrothermal atomic absorption spectroscopy detection using dicyclohexano-18-crown-6 as extractant system. *J. Hazard. Mater.* **167,** 597–601 (2009).

47. Bagheri, H. *et al.* Simultaneous electrochemical sensing of thallium, lead and mercury using a novel ionic liquid/graphene modified electrode. *Anal. Chim. Acta* **870,** 56–66 (2015).

48. Gabelica, V. in *Nucleic Acids Gas Phase* (Gabelica, V.) 3–20 (Springer Berlin Heidelberg, 2014). doi:10.1007/978-3-642-54842-0

49. Zhou, J., Battig, M. R. & Wang, Y. Aptamer-based molecular recognition for biosensor development. *Anal. Bioanal. Chem.* **398,** 2471–2480 (2010).

50. Monajjemi, M. & Chahkandi, B. Theoretical investigation of hydrogen bonding in Watson–Crick, Hoogestein and their reversed and other models: comparison and analysis for configurations of adenine–thymine base pairs in 9 models. *J. Mol. Struct. THEOCHEM* **714,** 43–60 (2005).

51. Iliuk, A. B., Hu, L. & Tao, W. A. Aptamer in Bioanalytical Applications. *Anal. Chem.* **83,** 4440–4452 (2011).

52. Yang, L. *et al.* Aptamer-conjugated nanomaterials and their applications. *Adv. Drug Deliv. Rev.* **63,** 1361–1370 (2011).

53. Gu, M. B. & Kim, H.-S. *Biosensors Based on Aptamers and Enzymes*. 13–14, 30–38, 125–128 (Springer Berlin Heidelberg, 2014).

54. Sefah, K. *et al.* Nucleic acid aptamers for biosensors and bio-analytical applications. *Analyst* **134,** 1765–1775 (2009).

55. Zhou, W., Huang, P.-J. J., Ding, J. & Liu, J. Aptamer-based biosensors for biomedical diagnostics. *Analyst* **139,** 2627–2640 (2014).

56. Long, F., Zhu, A. & Shi, H. Recent advances in optical biosensors for environmental monitoring and early warning. *Sensors (Basel).* **13,** 13928–13948 (2013).

57. Burge, S., Parkinson, G. N., Hazel, P., Todd, A. K. & Neidle, S. Quadruplex DNA: sequence, topology and structure. *Nucleic Acids Res.* **34,** 5402–15 (2006).

58. Banfalvi, G. STRUCTURAL ORGANIZATION OF DNA B-DNA. *Biochem. Educ.* **14,** 50–59 (1986).

59. Stoltenburg, R., Reinemann, C. & Strehlitz, B. SELEX--a (r)evolutionary method to generate high-affinity nucleic acid ligands. *Biomol. Eng.* **24,** 381–403 (2007).

60. Campbell, N. H. & Neidle, S. in *Interplay between Met. Ions Nucleic Acids* (Sigel, A., Sigel, H. & Sigel, R. K. O.) **10,** 29–39 (Springer Netherlands, 2012).

61. Huppert, J. L. Four-stranded nucleic acids: structure, function and targeting of G-quadruplexes. *Chem. Soc. Rev.* **37,** 1375 (2008).

62. Gray, R. D., Li, J., Chaires, J. B. & Louis, V. Energetics and Kinetics of a Conformational Switch in G-Quadruplex DNA. *J. Phys. Chem. B* 2676–2683 (2009).

63. Georgiades, S. N., Abd Karim, N. H., Suntharalingam, K. & Vilar, R. Interaction of Metal Complexes with G-Quadruplex DNA. *Angew. Chemie Int. Ed.* **49,** 4020–4034 (2010).

64. Ross, W. S., Hardin, C. C. & Carolina, N. Ion-Induced Stabilization of the G-DNA Quadruplex: Free Energy Perturbation Studies. *J. Am. Chem. Soc.* **116,** 6070–6080 (1994).

65. Bochman, M. L., Paeschke, K. & Zakian, V. DNA secondary structures: stability and function of G-quadruplex structures. *Nat. Rev. Genet.* **13,** 770–780 (2012).

66. Wong, A. & Wu, G. Selective Binding of Monovalent Cations to the Stacking G-Quartet Structure Formed by Guanosine 5 ′ -Monophosphate : A Solid-State NMR Study. *J. Am. Chem. Soc.* 13895–13905 (2003).

67. Wang, Z.-F., Li, M.-H., Hsu, S.-T. D. & Chang, T.-C. Structural basis of sodium-potassium exchange of a human telomeric DNA quadruplex without topological conversion. *Nucleic Acids Res.* **42,** 4723–4733 (2014).

68. Meng, F., Xu, W. & Liu, C. Molecular Design. *Internet Electron. J. Mol. Des.* **5,** 79–88 (2006).

69. Pagano, B., Mattia, C. A. & Giancola, C. Applications of isothermal titration calorimetry in biophysical studies of G-quadruplexes. *Int. J. Mol. Sci.* **10,** 2935–2957 (2009).

70. Smargiasso, N. *et al.* G-Quadruplex DNA Assemblies : Loop Length , Cation Identity , and Multimer Formation †. *J. Am. Chem. Soc.* **135,** 10208–10216 (2008).

71. Gill, M. L., Strobel, S. A. & Loria, J. P. Crystallization and characterization of the thallium form of the Oxytricha nova G-quadruplex. *Nucleic Acids Res.* **34,** 4506–14 (2006).

72. Ida, R. & Wu, G. Solid-state 87Rb NMR signatures for rubidium cations bound to a G-quadruplex. *Chem. Commun. (Camb).* 4294–6 (2005). doi:10.1039/b505674h

73. Cesare Marincola, F. *et al.* Competitive binding exchange between alkali metal ions (K+, Rb+, and Cs+) and Na+ ions bound to the dimeric quadruplex [d(G4T4G4)]2: a 23Na and 1H NMR study. *Magn. Reson. Chem.* **47,** 1036–1042 (2009).

74. Kwan, I. C. M., Mo, X., Wu, G. & Kl, C. Probing Hydrogen Bonding and Ion - Carbonyl Interactions by. *J. Am. Chem. Soc.* **129,** 2398–2407 (2007).

75. Liu, Y., Li, B., Cheng, D. & Duan, X. Simple and sensitive fluorescence sensor for detection of potassium ion in the presence of high concentration of sodium ion using berberine–G-quadruplex complex as sensing element. *Microchem. J.* **99,** 503–507 (2011).

76. Hardin, C. C., Perry, A. G. & White, K. Thermodynamic and Kinetic Characterization of the Dissociation and Assembly of Quadruplex Nucleic Acids. *Biopolym. (Nucleic Acid Sci.* **56,** 147–194 (2001).

77. Turdean, G. L. Design and Development of Biosensors for the Detection of Heavy Metal Toxicity. *Int. J. Electrochem.* **2011,** 1–15 (2011).

78. Xiang, Y. & Lu, Y. DNA as Sensors and Imaging Agents for Metal Ions. *Inorg. Chem.* **53,** 1925– 1942 (2014).

79. Xu, X., Wang, J., Jiao, K. & Yang, X. Colorimetric detection of mercury ion (Hg2+) based on DNA oligonucleotides and unmodified gold nanoparticles sensing system with a tunable detection range. *Biosens. Bioelectron.* **24,** 3153–8 (2009).

80. Freisinger, E. & Sigel, R. K. O. From nucleotides to ribozymes—A comparison of their metal ion binding properties. *Coord. Chem. Rev.* **251,** 1834–1851 (2007).

81. Sen, D. & Gilbert, W. A Sodium-Potassium switch in the formation of four stranded G4-DNA. *Nature* **344,** 410–414 (1990).

82. Breaker, R. R. & Joyce, G. F. A DNA enzyme that cleaves RNA. *Chem. Biol.* **1,** 223–229 (1994).

83. Qin, H., Ren, J., Wang, J., Luedtke, N. W. & Wang, E. G-Quadruplex-Modulated Fluorescence Detection of Potassium in the Presence of a 3500-Fold Excess of Sodium Ions. *Anal. Chem.* **82,** 8356–8360 (2010).

84. Li, T., Dong, S. & Wang, E. Label-Free Colorimetric Detection of Aqueous Mercury Ion (Hg 2 +) Using Hg 2 + -Modulated G-Quadruplex-Based DNAzymes. *Anal. Chem.* **81,** 2144–2149 (2009).

85. Juskowiak, B. Analytical potential of the quadruplex DNA-based FRET probes. *Anal. Chim. Acta* **568,** 171–180 (2006).

86. Li, T., Wang, E. & Dong, S. Lead (II) -Induced Allosteric G-Quadruplex DNAzyme as a Colorimetric and Chemiluminescence Sensor for Highly Sensitive and Selective Pb 2 + Detection. *Anal. Chem.* **82,** 1515–1520 (2010).

87. Noomnarm, U. & Clegg, R. M. Fluorescence lifetimes: fundamentals and interpretations. *Photosynth. Res.* **101,** 181–94 (2009).

88. Michalet, X. *et al.* The power and prospects of fluorescence microscopies and spectroscopies. *Annu. Rev. Biophys. Biomol. Struct.* **32,** 161–82 (2003).

89. Selvin, P. R. The renaissance of fluorescence resonance energy transfer. *Nat. Struct. Biol.* **7,** 730–734 (2000).

90. Clegg, R. M. Fluorescence resonance energy transfer. *Curr. Opin. Biotechnol.* **6,** 103–110 (1995).

91. Valeur, B. *Molecular Fluorescence: Principles and Applications*. **8,** 113 (Wiley-VCH Verlag GmbH, 2001).

92. Jares-Erijman, E. a & Jovin, T. M. FRET imaging. *Nat. Biotechnol.* **21,** 1387–1395 (2003).

93. Feng, C., Dai, S. & Wang, L. Optical aptasensors for quantitative detection of small biomolecules: a review. *Biosens. Bioelectron.* **59,** 64–74 (2014).

94. Cho, E. J., Lee, J.-W. & Ellington, A. D. Applications of aptamers as sensors. *Annu. Rev. Anal. Chem. (Palo Alto. Calif).* **2,** 241–264 (2009).

95. Li, H. & Rothberg, L. Colorimetric detection of DNA sequences based on electrostatic interactions with unmodified gold nanoparticles. *Proc. Natl. Acad. Sci.* **101,** 14036–14039 (2004).

96. Li, L., Li, B., Qi, Y. & Jin, Y. Label-free aptamer-based colorimetric detection of mercury ions in aqueous media using unmodified gold nanoparticles as colorimetric probe. *Anal. Bioanal. Chem.* **393,** 2051–2057 (2009).

97. Wang, L., Liu, X., Hu, X., Song, S. & Fan, C. Unmodified gold nanoparticles as a colorimetric probe for potassium DNA aptamers. *Chem. Commun. (Camb).* 3780–3782 (2006). doi:10.1039/b607448k

98. Wang, Z., Lee, J. H. & Lu, Y. Label-Free Colorimetric Detection of Lead Ions with a Nanomolar Detection Limit and Tunable Dynamic Range by using Gold Nanoparticles and DNAzyme. *Adv. Mater.* **20,** 3263–3267 (2008).

99. Liu, J. & Lu, Y. Preparation of aptamer-linked gold nanoparticle purple aggregates for colorimetric sensing of analytes. *Nat. Protoc.* **1,** 246–52 (2006).

100. Li, H. & Rothberg, L. J. Label-Free Colorimetric Detection of Specific Sequences in Genomic DNA Amplified by the Polymerase Chain Reaction increasingly important in clinical diagnosis , pathology , and. *J. Am. Chem. Soc.* **126,** 10958–10961 (2004).

101. Liu, J. Adsorption of DNA onto gold nanoparticles and graphene oxide: surface science and applications. *Phys. Chem. Chem. Phys.* **14,** 10485–10496 (2012).

102. Li, H. & Rothberg, L. J. DNA Sequence Detection Using Selective Fluorescence Quenching of Tagged Oligonucleotide Probes by Gold Nanoparticles. *Anal. Chem.* **76,** 5414–5417 (2004).

103. Li, D. I., Song, S. & Fan, C. Target-Responsive Structural Switching for Nucleic Acid-Based Sensors. *Acc. Chem. Res.* **43,** 631–641 (2010).

104. Rosi, N. L. & Mirkin, C. A. Nanostructures in Biodiagnostics. *Chem. Rev.* **105,** 1547–1562 (2005).

105. Zhao, W., Brook, M. a & Li, Y. Design of gold nanoparticle-based colorimetric biosensing assays. *Chembiochem* **9,** 2363–2371 (2008).

106. Gillard, R. D. Circular Dichroism. *Analyst* **88,** 825–828 (1963).

107. Ranjbar, B. & Gill, P. Circular dichroism techniques: biomolecular and nanostructural analyses- a review. *Chem. Biol. Drug Des.* **74,** 101–120 (2009).

108. Gottarelli, G. *et al.* Review Article The Use of Circular Dichroism Spectroscopy for Studying the Chiral Molecular Self-Assembly : An Overview. *Chirality* **485,** 471–485 (2008).

109. Ciuk, D. Review Article Circular Dichroism Spectroscopy of DNA : From Duplexes to. *Chirality* **698,** 691–698 (2012).

110. Gray, D. M. *et al.* Measured and Calculated CD Spectra of G-Quartets Stacked with the Same or Opposite Polarities. *Chirality* **440,** 431–440 (2008).

111. Nagatoishi, S., Tanaka, Y. & Tsumoto, K. Circular dichroism spectra demonstrate formation of the thrombin-binding DNA aptamer G-quadruplex under stabilizing-cation-deficient conditions. *Biochem. Biophys. Res. Commun.* **352,** 812–817 (2007).

112. Williamson, J. R. G-QUARTET STRUCTURES IN TELOMERIC DNA. *Annu. Rev. Biophys. Biomol. Struct.* **23,** 703–730 (1994).

113. Vorlíčková, M. *et al.* Circular dichroism and guanine quadruplexes. *Methods* **57,** 64–75 (2012).

114. Karsisiotis, A. I. *et al.* Topological characterization of nucleic acid G-quadruplexes by UV absorption and circular dichroism. *Angew. Chem. Int. Ed. Engl.* **50,** 10645–8 (2011).

115. Randazzo, A., Spada, G. P. & Webba, M. Circular Dichroism of Quadruplex Structures. *Top Curr Chem* **330,** 67–86 (2012).

116. Liu, W. *et al.* Kinetics and mechanism of G-quadruplex formation and conformational switch in a G-quadruplex of PS2.M induced by Pb^{2+}. *Nucleic Acids Res.* **40,** 4229–4236 (2012).

117. Shafer, R. H. Characterization of an Unusual Folding Pattern in a Catalytically Active Guanine Quadruplex Structure. *Biopolymers* **82,** 558–569 (2006).

118. Kong, D.-M., Wu, J., Wang, N., Yang, W. & Shen, H.-X. Peroxidase activity-structure relationship of the intermolecular four-stranded G-quadruplex-hemin complexes and their application in Hg2+ ion detection. *Talanta* **80,** 459–465 (2009).

119. Liu, Y. *et al.* An aptamer-based keypad lock system. *Chem. Commun. (Camb).* **48,** 802–804 (2012).

120. Li, R. *et al.* G-quadruplex DNAzymes-induced highly selective and sensitive colorimetric sensing of free heme in rat brain. *Analyst* **139,** 1993–1999 (2014).

121. Abe, H. *et al.* Structure formation and catalytic activity of DNA dissolved in organic solvents. *Angew. Chem. Int. Ed. Engl.* **51,** 6475–6479 (2012).

122. Lim, K. W., Amrane, S., Bouaziz, S., Xu, W. & Mu, Y. Structure of the Human Telomere in K + Solution : A Stable Basket-Type G-Quadruplex with Only Two G-Tetrad Layers. *J. Am. Chem. Soc.* **301,** 4301–4309 (2015).

123. Li, W., Hou, X., Wang, P., Xi, X. & Li, M. Direct Measurement of Sequential Folding Pathway and Energy Landscape of Human Telomeric G - quadruplex Structures. *J. Am. Chem. Soc.* **135,** 10–13 (2013).

124. Freire, E., Mayorga, O. L. & Straume, M. Isothermal Titration. *Anal. Chem.* **62,** (1990).

125. Lewis, E. A. & Murphy, K. P. Isothermal Titration Calorimetry. *Methods Mol. Biol.* **305,** 1–15 (2005).

126. Lopez, M. M. & Makhatadze, G. I. Isothermal Titration Calorimetry. *Methods Mol. Biol.* **173,** 121–126 (2002).